

MONKES: a fast neoclassical code for the evaluation of monoenergetic transport coefficients

F. J. Escoto¹, J. L. Velasco¹, I. Calvo¹, M. Landreman² and F. I. Parra³

¹Laboratorio Nacional de Fusión, CIEMAT, 28040 Madrid, Spain

²University of Maryland, College Park, MD 20742, USA

³Princeton Plasma Physics Laboratory, Princeton, NJ 08540, USA

E-mail: fjavier.escoto@ciemat.es

April 2023

Abstract. MONKES is a new neoclassical code for the evaluation of monoenergetic transport coefficients in large aspect ratio stellarators. By means of a convergence study and benchmarks with other codes, it is shown that MONKES is accurate and efficient. The combination of spectral discretization in spatial and velocity coordinates with block sparsity allows MONKES to compute monoenergetic coefficients at low collisionality, in a single processor, in approximately one minute. MONKES is sufficiently fast to be integrated into stellarator optimization codes for direct optimization of the bootstrap current and to be included in predictive transport suites.

Keywords: stellarator optimization, neoclassical transport, bootstrap current.
Submitted to: *Nucl. Fusion*

1. Introduction

Stellarators are an attractive alternative to tokamaks as future fusion reactors. While tokamaks require a large toroidal current to generate part of the magnetic field, in stellarators the field is produced entirely by external magnets. As a consequence, stellarators avoid current-induced instabilities and facilitate steady-state operation. These advantages come at the expense of making the magnetic field three-dimensional. In tokamaks, axisymmetry guarantees that the radial displacement that charged particles experience along their collisionless orbits averages to zero. Therefore, in the absence of collisions, all charged particles are confined. However, in a generic stellarator the orbit-averaged radial drift velocity does not vanish for trapped particles and they quickly drift out of the device. The combination of a non zero orbit-averaged radial drift and a small collision frequency (reactor-relevant fusion plasmas are weakly collisional in the core) produces, for a generic stellarator, intolerably large levels of neoclassical transport.

Hence, stellarator magnetic fields must be carefully designed in order to display good confinement properties. This process of tailoring of the magnetic field is called stellarator optimization. The goal of neoclassical optimization is to obtain a stellarator with levels of neoclassical losses equivalent or lower to those in an axisymmetric device. Stellarator magnetic fields in which the orbit-averaged radial magnetic drift is zero for all particles are called omnigenous [1]. Thus, the goal of neoclassical optimization is to obtain magnetic fields which are close to omnigenicity. However, addressing only radial transport in the optimization process is not sufficient. In toroidal plasmas, the parallel flow of electrons and the rest of species is not, in general, balanced. This mismatch produces a net parallel current at each flux surface which, through Ampère's law, modifies the magnetic field \mathbf{B} . When the current is generated by neoclassical mechanisms and non-zero plasma profile gradients, we speak of bootstrap current. The bootstrap current and its effect on the magnetic configuration must be taken into account in the design of optimized stellarator magnetic fields.

Two different subclasses of omnigenous stellarators have drawn particular attention: quasi-isodynamic (QI) and quasi-symmetric (QS) stellarators. Quasi-isodynamic configurations are omnigenous configurations in which the curves of constant magnetic field strength $B := |\mathbf{B}|$ on a flux surface close poloidally. This additional property has an important implication: QI stellarators produce zero bootstrap current at low collisionality [2, 3]. Thanks to this feature, QI stellarators can control plasma-wall interaction by means of a divertor relying on a specific structure of islands, which could not be realized in the presence of large

toroidal currents. The Wendelstein 7-X (W7-X) experiment was designed to be close to QI and demonstrates that theoretically based stellarator optimization can be applied to construct a device with much better confinement properties than any previous stellarator [4]. Moreover, the bootstrap current produced in W7-X plasmas is smaller than in non optimized machines [5]. However, despite its success, there is still room for improvement. The two main configurations of W7-X, the KJM (or so-called “high mirror”) and the EIM (also known as “standard”) are not optimized for simultaneously having low levels of radial and parallel transport [6, 4]: While W7-X EIM has very small radial transport, it has intolerably large bootstrap current. Conversely, W7X-KJM displays small bootstrap current but larger levels of radial transport. Consequently, optimization of QI stellarators is a very active branch of research and enormous effort has been put in pushing forward the design and construction of quasi-isodynamic stellarators [7, 8, 9, 10, 11].

The QS subclass of omnigenous configurations is attractive as the neoclassical properties of such magnetic fields are isomorphic to those in a tokamak [12, 13]. Recently, it has been shown that it is possible to design QS magnetic fields with extremely low neoclassical losses [14]. In contrast to QI configurations, QS stellarators are expected to have a substantial bootstrap current[‡] and its effect must be taken into account [16]. Examples of this subclass are the Helically Symmetric eXperiment (HSX) [17] or the design National Compact Stellarator Experiment (NCSX) [18].

Typically, at each iteration of the optimization process a large number ($\sim 10^2$) of magnetic configurations are generated. Therefore, in order to neoclassically optimize magnetic fields it is required to be able to evaluate fast the neoclassical properties of each configuration. Due to this requirement, neoclassical properties are typically addressed indirectly. For instance, one can tailor the variation of the magnetic field strength B on the flux-surface so that it nearly fulfills quasi-isodinamicity: the isolines of B can be made close poloidally and the variance of the extrema of B along field lines can be minimized.

A different approach relies on figures of merit, which are easy to calculate, for specific collisional regimes. For the $1/\nu$ regime, the code NEO [19] computes the effective ripple ϵ_{eff} , which encapsulates the dependence of radial neoclassical transport on the magnetic configuration. For transport within the flux surface, there exist long mean free path formulae for parallel flow and bootstrap current [20, 21, 22].

[‡] With the exception of the quasi-poloidally symmetric magnetic field, which lies at the intersection of QI and QS configurations. However, quasi-poloidal symmetry is impossible to achieve near the magnetic axis, see e.g. [15].

Although they can be computed very fast and might capture some qualitative behaviour, these formulae are plagued with noise due to resonances in rational surfaces and, even with smoothing ad-hoc techniques, they are not accurate [16]. This lack of accuracy limits their application for optimization purposes. During the optimization process, an accurate calculation of the bootstrap current is required to account for its effect (e.g. for optimizing QS stellarators) or to keep it sufficiently small (when optimizing for quasi-isodynamicity). Recent developments allow direct optimization of radial neoclassical transport. Based on rigorous derivations [23, 24], the code KNOSOS [25, 26] solves very fast an orbit-averaged drift-kinetic equation that is accurate for low collisionality regimes. KNOSOS is included in the stellarator optimization suite STELOPT [27] and in the predictive transport frameworks TANGO [28] and TRINITY [29].

In this work we present MONKES (MONoenergetic Kinetic Equation Solver), a new neoclassical code conceived to satisfy the necessity of fast and accurate calculations of the bootstrap current for stellarator optimization. Specifically, MONKES makes it possible to include among the optimization targets the monoenergetic coefficients \hat{D}_{ij} where $i, j \in \{1, 2, 3\}$ (their precise definition is given in section 2). These nine coefficients encapsulate the neoclassical transport across and within flux surfaces. The parallel flow of each species can be calculated in terms of the coefficients \hat{D}_{3j} . In the absence of externally applied loop voltage, the bootstrap current is driven by the radial electric field and gradients of density and temperature. The so-called bootstrap current coefficient \hat{D}_{31} is the one that relates the parallel flow to these gradients. The six remaining coefficients \hat{D}_{ij} for $i \in \{1, 2\}$ allow to compute the flux of particles and heat across the flux surface. Since MONKES also computes fast the radial transport coefficients at low collisionality (however, not as fast as the orbit-averaged code KNOSOS), it can be used to optimize taking into account the $1/\nu$ and $\sqrt{\nu}$ regimes. Additionally, it can compute much faster (~ 1 second) the $1/\nu$ to plateau transition (something that KNOSOS cannot do). Apart from optimization, MONKES can find many other applications. For instance, it can be used for the analysis of experimental discharges or also be included in predictive transport frameworks.

This paper is organized as follows: in section 2, we introduce the drift-kinetic equation solved by MONKES and the transport coefficients that it computes. In section 3, we explain the algorithm used to solve the drift-kinetic equation and its implementation. In section 4, by means of a convergence study, we demonstrate that MONKES can be used to compute accurate monoenergetic coefficients at low collisionality

very fast for the $1/\nu$ and $\sqrt{\nu}$ regimes. MONKES results are also benchmarked against DKES [30] and, when necessary, against SFINCS [31]. Finally, in section 5 we summarize the results and discuss future lines of work.

2. Drift-kinetic equation and transport coefficients

MONKES solves the drift-kinetic equation

$$(v\xi\mathbf{b} + \mathbf{v}_E) \cdot \nabla h_a + v\nabla \cdot \mathbf{b} \frac{(1 - \xi^2)}{2} \frac{\partial h_a}{\partial \xi} - \nu^a \mathcal{L} h_a = S_a, \quad (1)$$

where $\mathbf{b} := \mathbf{B}/B$ is the unitary vector tangent to magnetic field lines and we have employed as velocity coordinates the cosine of the pitch-angle $\xi := \mathbf{v} \cdot \mathbf{b}/|\mathbf{v}|$ and the magnitude of the velocity $v := |\mathbf{v}|$.

We assume that the magnetic configuration has nested flux-surfaces. We denote by $\psi \in [0, \psi_{\text{lcf}}]$ a radial coordinate that labels flux-surfaces, where ψ_{lcf} denotes the label of the last closed flux-surface. In equation (1), h_a is the non-adiabatic component of the deviation of the distribution function from a local Maxwellian for a plasma species a

$$f_{\text{Ma}}(\psi, v) := n_a(\psi) \pi^{-3/2} v_{ta}^{-3}(\psi) \exp\left(-\frac{v^2}{v_{ta}^2(\psi)}\right). \quad (2)$$

Here, n_a is the density of species a , $v_{ta} := \sqrt{2T_a/m_a}$ is its thermal velocity, T_a its temperature (in energy units) and m_a its mass.

For the convective term in equation (1)

$$\mathbf{v}_E := \frac{\mathbf{E}_0 \times \mathbf{B}}{\langle B^2 \rangle} = -E_\psi(\psi) \frac{\mathbf{B} \times \nabla \psi}{\langle B^2 \rangle} \quad (3)$$

denotes the incompressible $\mathbf{E} \times \mathbf{B}$ drift approximation [24] and $\mathbf{E}_0 = E_\psi(\psi) \nabla \psi$ is the electrostatic piece of the electric field \mathbf{E} perpendicular to the flux-surface. The symbol $\langle \dots \rangle$ stands for the flux-surface average operation. Denoting by $V(\psi)$ to the volume enclosed by the flux-surface labelled by ψ , the flux-surface average of a function f can be defined as the limit

$$\langle f \rangle := \lim_{\delta\psi \rightarrow 0} \frac{\int_{V(\psi+\delta\psi)} f d^3\mathbf{r} - \int_{V(\psi)} f d^3\mathbf{r}}{V(\psi+\delta\psi) - V(\psi)}, \quad (4)$$

where $d^3\mathbf{r}$ is the spatial volume form.

We denote the Lorentz pitch-angle scattering operator by \mathcal{L} , which in coordinates (ξ, v) takes the form

$$\mathcal{L} := \frac{1}{2} \frac{\partial}{\partial \xi} \left((1 - \xi^2) \frac{\partial}{\partial \xi} \right). \quad (5)$$

In the collision operator, $\nu^a(v) = \sum_b \nu^{ab}(v)$ and

$$\nu^{ab}(v) := \frac{4\pi n_b e_a^2 e_b^2}{m_a^2 v_{ta}^3} \log \Lambda \frac{\text{erf}(v/v_{tb}) - G(v/v_{tb})}{v^3/v_{ta}^3} \quad (6)$$

stands for the pitch-angle collision frequency between species a and b . We denote the respective charges of each species by e_a and e_b , the Chandrasekhar function by $G(x) = [\text{erf}(x) - (2x/\sqrt{\pi}) \exp(-x^2)] / (2x^2)$, $\text{erf}(x)$ is the error function and $\log \Lambda$ is the Coulomb logarithm [32].

On the right-hand-side of equation (1)

$$S_a := -\mathbf{v}_{ma} \cdot \nabla \psi \left(A_{1a} + \frac{v^2}{v_{ta}^2} A_{2a} \right) f_{Ma} + Bv\xi A_{3a} f_{Ma} \quad (7)$$

is the source term,

$$\mathbf{v}_{ma} \cdot \nabla \psi = -\frac{Bv^2}{\Omega_a} \frac{1 + \xi^2}{2B^3} \mathbf{B} \times \nabla \psi \cdot \nabla B \quad (8)$$

is the expression of the radial magnetic drift assuming ideal magnetohydrodynamical equilibrium, $\Omega_a = e_a B / m_a$ is the gyrofrequency of species a , e_a its charge and the flux functions

$$A_{1a}(\psi) := \frac{d \ln n_a}{d\psi} - \frac{3}{2} \frac{d \ln T_a}{d\psi} - \frac{e_a E_\psi}{T_a}, \quad (9)$$

$$A_{2a}(\psi) := \frac{d \ln T_a}{d\psi}, \quad (10)$$

$$A_{3a}(\psi) := \frac{e_a \langle \mathbf{E} \cdot \mathbf{B} \rangle}{T_a \langle B^2 \rangle}, \quad (11)$$

are the so-called thermodynamical forces.

Mathematically speaking, there are still two additional conditions to completely determine the problem to be solved. First, equation (1) must be solved imposing regularity conditions at $\xi = \pm 1$

$$\left((1 - \xi^2) \frac{\partial h_a}{\partial \xi} \right) \Big|_{\xi=\pm 1} = 0. \quad (12)$$

In the second place, as the differential operator on the left-hand-side of equation (1) has a non trivial kernel, the solution to equation (1) is determined up to an additive function $g(\psi, v)$. This function is unimportant as it does not contribute to the neoclassical transport quantities of interest. Nevertheless, in order to have a unique solution to the drift-kinetic equation, it must be fixed by imposing an appropriate additional constraint. We will select this free function (for fixed (ψ, v)) by imposing

$$\left\langle \int_{-1}^1 h_a d\xi \right\rangle = C, \quad (13)$$

for some $C \in \mathbb{R}$ that will be determined in section 3.

The drift-kinetic equation (1) is the one presented in [33]. An equivalent form of this equation is solved by the standard neoclassical code DKES using a variational principle. Although the main feature of the code SFINCS is to solve a more complete neoclassical drift-kinetic equation, it can also solve equation (1).

Taking the moments $\{\mathbf{v}_{ma} \cdot \nabla \psi, (v^2/v_{ta}^2) \mathbf{v}_{ma} \cdot \nabla \psi, v\xi B\}$ of h_a and then the flux-surface average yields, respectively, the radial particle flux, the radial heat flux and the parallel flow

$$\langle \mathbf{r}_a \cdot \nabla \psi \rangle := \left\langle \int \mathbf{v}_{ma} \cdot \nabla \psi h_a d^3 \mathbf{v} \right\rangle, \quad (14)$$

$$\left\langle \frac{\mathbf{Q}_a \cdot \nabla \psi}{T_a} \right\rangle := \left\langle \int \frac{v^2}{v_{ta}^2} \mathbf{v}_{ma} \cdot \nabla \psi h_a d^3 \mathbf{v} \right\rangle, \quad (15)$$

$$\frac{\langle n_a \mathbf{V}_a \cdot \mathbf{B} \rangle}{B_0} := \left\langle \frac{B}{B_0} \int v\xi h_a d^3 \mathbf{v} \right\rangle, \quad (16)$$

where $B_0(\psi)$ is a reference value for the magnetic field strength on the flux-surface (its explicit definition is given in section 3).

It is a common practice for linear drift-kinetic equations (e.g. [33], [6], [31]) to apply superposition and split h_a into several additive terms. As in the drift-kinetic equation (1) there are no derivatives or integrals along ψ nor v , it is convenient to use the splitting

$$h_a = f_{Ma} \left[\frac{Bv}{\Omega_a} \left(A_{1a} f_1 + A_{2a} \frac{v^2}{v_{ta}^2} f_2 \right) + B_0 A_{3a} f_3 \right]. \quad (17)$$

The splitting is chosen so that the functions $\{f_j\}_{j=1}^3$ are solutions to

$$\xi \mathbf{b} \cdot \nabla f_j + \nabla \cdot \mathbf{b} \frac{(1 - \xi^2)}{2} \frac{\partial f_j}{\partial \xi} - \frac{\hat{E}_\psi}{\langle B^2 \rangle} \mathbf{B} \times \nabla \psi \cdot \nabla f_j - \hat{\nu} \mathcal{L} f_j = s_j, \quad (18)$$

for $j = 1, 2, 3$, where $\hat{\nu} := \nu(v)/v$ and $\hat{E}_\psi := E_\psi/v$. The source terms are defined as

$$s_1 := -\mathbf{v}_{ma} \cdot \nabla \psi \frac{\Omega_a}{Bv^2}, \quad s_2 := s_1, \quad s_3 := \xi \frac{B}{B_0}. \quad (19)$$

Note that each source s_j corresponds to one of the three summands of the right hand side of definition (7).

The relation between h_a and f_j given by equation (17) is such that the transport quantities (14), (15) and (16) can be written in terms of four transport coefficients which, for fixed $(\hat{\nu}, \hat{E}_\psi)$, depend only on the magnetic configuration. As $d\hat{\nu}/dv$ never annuls, the dependence of f_j on the velocity v can be parametrized by its dependence on $\hat{\nu}$. Thus, for fixed $(\hat{\nu}, \hat{E}_\psi)$, equation (18) is completely determined by the magnetic configuration. Hence, its unique solutions f_j that satisfy conditions (12) and (13) are also completely determined by the magnetic configuration.

The ad-hoc assumptions that lead to ψ and v appearing as parameters in the drift-kinetic equation (1) comprise the so called local monoenergetic approximation to neoclassical transport (see e.g. [34]).

Using splitting (17) we can write the transport quantities (14), (15) and (16) in terms of the Onsager matrix

$$\begin{bmatrix} \langle \mathbf{\Gamma}_a \cdot \nabla \psi \rangle \\ \langle \frac{\mathbf{Q}_a \cdot \nabla \psi}{T_a} \rangle \\ \langle \frac{n_a \mathbf{V}_a \cdot \mathbf{B}}{B_0} \rangle \end{bmatrix} = \begin{bmatrix} L_{11a} & L_{12a} & L_{13a} \\ L_{21a} & L_{22a} & L_{23a} \\ L_{31a} & L_{32a} & L_{33a} \end{bmatrix} \begin{bmatrix} A_{1a} \\ A_{2a} \\ A_{3a} \end{bmatrix}. \quad (20)$$

Here, we have defined the thermal transport coefficients as

$$L_{ija} := \int_0^\infty 2\pi v^2 f_{Ma} w_i w_j D_{ija} dv, \quad (21)$$

where $w_1 = w_3 = 1$, $w_2 = v^2/v_{ta}^2$ and we have used that $\int g d^3\mathbf{v} = 2\pi \int_0^\infty \int_{-1}^1 g v^2 d\xi dv$ for any integrable function $g(\xi, v)$. The quantities D_{ija} are defined as

$$D_{ija} := -\frac{B^2 v^3}{\Omega_a^2} \hat{D}_{ij}, \quad i, j \in \{1, 2\}, \quad (22)$$

$$D_{i3a} := -\frac{B_0 B v^2}{\Omega_a} \hat{D}_{i3}, \quad i \in \{1, 2\}, \quad (23)$$

$$D_{3ja} := \frac{B v^2}{\Omega_a} \hat{D}_{3j}, \quad j \in \{1, 2\}, \quad (24)$$

$$D_{33a} := v B_0 \hat{D}_{33}, \quad (25)$$

where

$$\hat{D}_{ij}(\psi, v) := \left\langle \int_{-1}^1 s_i f_j d\xi \right\rangle, \quad i, j \in \{1, 2, 3\} \quad (26)$$

are the monoenergetic geometric coefficients. Note that, unlike D_{ija} , the monoenergetic geometric coefficients \hat{D}_{ij} do not depend on the species for fixed \hat{v} (however the correspondent value of v associated to each \hat{v} varies between species) and depend only on the magnetic geometry. In general, four independent monoenergetic geometric coefficients can be obtained by solving (18): \hat{D}_{11} , \hat{D}_{13} , \hat{D}_{31} and \hat{D}_{33} . However, when the magnetic field possesses stellarator symmetry or there is no radial electric field, only three of them are independent, as Onsager symmetry implies $\hat{D}_{13} = -\hat{D}_{31}$. Hence, obtaining the transport coefficients for all species requires to solve (18) for two different source terms s_1 and s_3 . The algorithm for solving equation (18) is described in section 3.

Finally, we briefly comment on the validity of the coefficients provided by equation (18) for the calculation of the bootstrap current. The pitch-angle scattering collision operator used in equation (1) lacks

parallel momentum conservation, i.e. $\int v \xi \nu^a \mathcal{L} F_a d^3\mathbf{v}$ is not identically zero. This lack of conservation introduces an spurious parallel force in the macroscopic momentum equation that can be obtained from kinetic equation (1). Besides, the pitch-angle scattering operator is not adequate for calculating parallel flow of electrons, which is a quantity required to compute the bootstrap current. Hence, in principle, the parallel transport directly predicted by equation (1) is not correct. Fortunately, there exist techniques (see e.g. [35] or [36]) to calculate the radial and parallel transport associated to more accurate momentum conserving collision operators by just solving the simplified drift-kinetic equation (18). This has been done successfully in the past by the code PENTA [37, 38], using the results of DKES. Nevertheless, the momentum restoring technique is not needed for minimizing the bootstrap current. In the method presented in section V of [36], when there is no net parallel inductive electric field (i.e. $A_{3a} = 0$), the parallel flow with the correct collision operator for any species vanishes when two integrals in v of \hat{D}_{31} vanish. Thus, minimizing \hat{D}_{31} translates in a minimization of the parallel flows of all species involved in the bootstrap current calculation, and therefore a minimization of this current.

3. Numerical method

In this section we describe the algorithm to numerically solve the drift-kinetic equation (18) and its implementation. The algorithm, based on the tridiagonal representation of the drift-kinetic equation, merges naturally when the velocity coordinate ξ is discretized using a Legendre spectral method.

First, in subsection 3.1 we will present the algorithm in a formal and abstract manner which is valid for any set of spatial coordinates. Nevertheless, for convenience in the discussion, we will use (right-handed) Boozer coordinates $(\psi, \theta, \zeta) \in [0, \psi_{lcs}] \times [0, 2\pi) \times [0, 2\pi/N_p)$. The integer $N_p \geq 1$ denotes the number of toroidal periods of the device. The radial coordinate is selected so that $2\pi\psi$ is the toroidal flux of the magnetic field and θ, ζ are respectively the poloidal and toroidal (in a single period) angles. In these coordinates, the magnetic field can be written as

$$\begin{aligned} \mathbf{B} &= \nabla\psi \times \nabla\theta - \iota(\psi) \nabla\psi \times \nabla\zeta \\ &= B_\psi(\psi, \theta, \zeta) \nabla\psi + B_\theta(\psi) \nabla\theta + B_\zeta(\psi) \nabla\zeta, \end{aligned} \quad (27)$$

and the Jacobian of the transformation reads

$$\sqrt{g}(\psi, \theta, \zeta) := (\nabla\psi \times \nabla\theta \cdot \nabla\zeta)^{-1} = \frac{B_\zeta + \iota B_\theta}{B^2}, \quad (28)$$

where $\iota := \mathbf{B} \cdot \nabla\theta / \mathbf{B} \cdot \nabla\zeta$ is the rotational transform. The flux-surface average operation (4) is written in

Boozer angles as

$$\langle f \rangle = \frac{dV^{-1}}{d\psi} \oint \oint f \sqrt{g} d\theta d\zeta. \quad (29)$$

We define§ the aforementioned reference value for the magnetic field strength B_0 on the flux-surface introduced in definition (16) as the $(0, 0)$ Fourier mode of the magnetic field strength. Namely,

$$B_0(\psi) := \frac{1}{4\pi^2 N_p} \oint \oint B(\psi, \theta, \zeta) d\theta d\zeta. \quad (30)$$

Using (27) and (28), the spatial differential operators present in the drift-kinetic equation (18) can be expressed in these coordinates as

$$\mathbf{b} \cdot \nabla = \frac{B}{B_\zeta + \iota B_\theta} \left(\iota \frac{\partial}{\partial \theta} + \frac{\partial}{\partial \zeta} \right), \quad (31)$$

$$\mathbf{B} \times \nabla \psi \cdot \nabla = \frac{B^2}{B_\zeta + \iota B_\theta} \left(B_\zeta \frac{\partial}{\partial \theta} - B_\theta \frac{\partial}{\partial \zeta} \right). \quad (32)$$

After the explanation of the algorithm, in subsection 3.2 its implementation in MONKES is described. In order to ease the notation, in subsections 3.1 and 3.2, we drop the subscript j that labels every different source term when possible. Also, as ψ and v act as mere parameters, we will omit their dependence and functions of these two variables will be referred to as constants.

3.1. Legendre polynomial expansion

The algorithm is based on the approximate representation of the distribution function f in a truncated Legendre series. We will search for approximate solutions to equation (18) of the form

$$f(\theta, \zeta, \xi) = \sum_{k=0}^{N_\xi} f^{(k)}(\theta, \zeta) P_k(\xi), \quad (33)$$

where $f^{(k)} = \langle f, P_k \rangle_{\mathcal{L}} / \langle P_k, P_k \rangle_{\mathcal{L}}$ is the k -th Legendre mode of $f(\theta, \zeta, \xi)$ (see Appendix A) and N_ξ is an integer greater or equal to 1. As mentioned in Appendix A, the usage of the expansion on Legendre polynomials (33) ensures that the regularity conditions (12) are satisfied. Of course, in general, the exact solution to equation (18) does not have a finite Legendre spectrum, but taking N_ξ sufficiently high in expansion (33) yields an approximate solution to the desired degree of accuracy (in infinite precision arithmetic).

In Appendix A we derive explicitly the projection of each term of the drift-kinetic equation (18) onto

§ Other definitions could be, for example, $\langle B \rangle$ or $\sqrt{\langle B^2 \rangle}$. Nevertheless, these definitions are equal in the large aspect ratio limit.

the Legendre basis when the representation (33) is used. When doing so, we obtain that the Legendre modes of the drift-kinetic equation have the tridiagonal representation

$$L_k f^{(k-1)} + D_k f^{(k)} + U_k f^{(k+1)} = s^{(k)}, \quad (34)$$

for $k = 0, 1, \dots, N_\xi$, where we have defined for convenience $f^{(-1)} := 0$ and from expansion (33) is clear that $f^{(N_\xi+1)} = 0$. Analogously to (33) the source term is expanded as $s = \sum_{k=0}^{N_\xi} s^{(k)} P_k$, and for the sources (19) this expansion is exact when $N_\xi \geq 2$. The spatial differential operators read

$$L_k = \frac{k}{2k-1} \left(\mathbf{b} \cdot \nabla + \frac{k-1}{2} \mathbf{b} \cdot \nabla \ln B \right), \quad (35)$$

$$D_k = -\frac{\hat{E}_\psi}{\langle B^2 \rangle} \mathbf{B} \times \nabla \psi \cdot \nabla + \frac{k(k+1)}{2} \hat{\nu}, \quad (36)$$

$$U_k = \frac{k+1}{2k+3} \left(\mathbf{b} \cdot \nabla - \frac{k+2}{2} \mathbf{b} \cdot \nabla \ln B \right). \quad (37)$$

Thanks to its tridiagonal structure, the system of equations (34) can be inverted using the standard Gaussian elimination algorithm for block tridiagonal matrices. Before introducing the algorithm we will explain how to fix the free constant of the solution to equation (34) so that it can be inverted. Note that the aforementioned kernel of the drift-kinetic equation translates in the fact that $f^{(0)}$ is not completely determined from equation (34). To prove this, we inspect the modes $k = 0$ and $k = 1$ that involve $f^{(0)}$. From expression (32) we can deduce that the term $D_0 f^{(0)} + U_0 f^{(1)}$ is invariant if we add to $f^{(0)}$ any function of $B_\theta \zeta + B_\zeta \theta$. For $\hat{E}_\psi \neq 0$, functions of $B_\theta \zeta + B_\zeta \theta$ lie in the kernel of $\mathbf{B} \times \nabla \psi \cdot \nabla$ and for $\hat{E}_\psi = 0$, D_0 is identically zero. Besides, the term $L_1 f^{(0)} + D_1 f^{(1)} + U_1 f^{(2)}$ remains invariant if we add to $f^{(0)}$ any function of $\theta - \iota \zeta$ (the kernel of $L_1 = \mathbf{b} \cdot \nabla$ is comprised of these functions). Thus, equation (34) is unaltered when we add to $f^{(0)}$ any constant (a function that belongs simultaneously to the kernels of $\mathbf{B} \times \nabla \psi \cdot \nabla$ and $\mathbf{b} \cdot \nabla$). A constraint equivalent to condition (13) is to fix the value of the 0-th Legendre mode of the distribution function at a single point of the flux-surface. For example,

$$f^{(0)}(0, 0) = 0, \quad (38)$$

which implicitly fixes the value of the constant C in (13). With this condition, equation (34) has a unique solution and its left-hand-side can be inverted (further details on its invertibility are given in Appendix B) to solve for $f^{(k)}$. Note that, as expansion (33) is finite and representation (34) is non diagonal, the functions $f^{(k)}$ obtained from inverting (34) constrained by (38) are approximations to the first $N_\xi + 1$ Legendre modes

of the exact solution to (18) satisfying (13) (further details at the end of Appendix A).

The algorithm for solving the truncated drift-kinetic equation (34) consists of two steps.

(i) **Forward elimination**

Starting from $\Delta_{N_\xi} = D_{N_\xi}$ and $\sigma^{(N_\xi)} = s^{(N_\xi)}$ we can obtain recursively the operators

$$\Delta_k = D_k - U_k \Delta_{k+1}^{-1} L_{k+1}, \quad (39)$$

and the sources

$$\sigma^{(k)} = s^{(k)} - U_k \Delta_{k+1}^{-1} \sigma^{(k+1)}, \quad (40)$$

for $k = N_\xi - 1, N_\xi - 2, \dots, 0$ (in this order). Equations (39) and (40) define the forward elimination. With this procedure we can transform equation (34) to the equivalent system

$$L_k f^{(k-1)} + \Delta_k f^{(k)} = \sigma^{(k)}, \quad (41)$$

for $k = 0, 1, \dots, N_\xi$. Note that this process corresponds to perform formal Gaussian elimination over

$$\left[\begin{array}{ccc|c} L_k & D_k & U_k & s^{(k)} \\ 0 & L_{k+1} & \Delta_{k+1} & \sigma^{(k+1)} \end{array} \right], \quad (42)$$

to eliminate U_k in the first row.

(ii) **Backward substitution**

Once we have the system of equations in the form (41) it is immediate to solve recursively

$$f^{(k)} = \Delta_k^{-1} \left(\sigma^{(k)} - L_k f^{(k-1)} \right), \quad (43)$$

for $k = 0, 1, \dots, N_\xi$ (in this order). Here, we denote by $\Delta_0^{-1} \sigma^{(0)}$ to the unique solution to $\Delta_0 f^{(0)} = \sigma^{(0)}$ that satisfies (38). As $L_1 = \mathbf{b} \cdot \nabla$, using expression (31), it is apparent from equation (43) that the integration constant does not affect the value of $f^{(1)}$.

We can apply this algorithm to solve equation (18) for f_1 , f_2 and f_3 in order to compute approximations to the transport coefficients. In terms of the Legendre modes of f_1 , f_2 and f_3 , the monoenergetic geometric coefficients from definition (26) read

$$\widehat{D}_{11} = 2 \left\langle s_1^{(0)} f_1^{(0)} \right\rangle + \frac{2}{5} \left\langle s_1^{(2)} f_1^{(2)} \right\rangle, \quad (44)$$

$$\widehat{D}_{31} = \frac{2}{3} \left\langle \frac{B}{B_0} f_1^{(1)} \right\rangle, \quad (45)$$

$$\widehat{D}_{13} = 2 \left\langle s_1^{(0)} f_3^{(0)} \right\rangle + \frac{2}{5} \left\langle s_1^{(2)} f_3^{(2)} \right\rangle, \quad (46)$$

$$\widehat{D}_{33} = \frac{2}{3} \left\langle \frac{B}{B_0} f_3^{(1)} \right\rangle, \quad (47)$$

where $3s_1^{(0)}/2 = 3s_1^{(2)} = \mathbf{B} \times \nabla \psi \cdot \nabla B / B^3$. Note from expressions (44), (45), (46) and (47) that, in order

to compute the monoenergetic geometric coefficients \widehat{D}_{ij} , we only need to calculate the Legendre modes $k = 0, 1, 2$ of the solution and we can stop the backward substitution (43) at $k = 2$. In the next subsection we will explain how MONKES solves equation (34) using this algorithm.

3.2. *Spatial discretization and algorithm implementation*

The algorithm described above allows, in principle, to compute the exact solution to the truncated drift-kinetic equation (34) which is an approximate solution to (18). However, to our knowledge, it is not possible to give an exact expression for the operator Δ_k^{-1} except for $k = N_\xi \geq 1$. Instead, we are forced to compute an approximate solution to (34). In order to obtain an approximate solution of equation (34) we assume that each $f^{(k)}$ has a finite Fourier spectrum so that it can be expressed as

$$f^{(k)}(\theta, \zeta) = \mathbf{I}(\theta, \zeta) \cdot \mathbf{f}^{(k)}, \quad (48)$$

where the Fourier interpolant row vector map $\mathbf{I}(\theta, \zeta)$ is defined at Appendix C and the column vector $\mathbf{f}^{(k)} \in \mathbb{R}^{N_{\text{fs}}}$ contains $f^{(k)}$ evaluated at the equispaced grid points

$$\theta_i = 2\pi i / N_\theta, \quad i = 0, 1, \dots, N_\theta - 1, \quad (49)$$

$$\zeta_j = 2\pi j / (N_\zeta N_p), \quad j = 0, 1, \dots, N_\zeta - 1. \quad (50)$$

Here, $N_{\text{fs}} := N_\theta N_\zeta$ is the number of points in which we discretize the flux-surface being N_θ and N_ζ respectively the number of points in which we divide the domains of θ and ζ . The solution to equation (34) in general has an infinite Fourier spectrum and cannot exactly be written as (48) but, taking sufficiently large values of N_θ and N_ζ , we can approximate the solution to equation (34) to arbitrary degree of accuracy (in infinite precision arithmetic). As is explained in Appendix C, introducing the Fourier interpolant (48) in equation (34) and then evaluating the result at the grid points, we obtain a system of $N_{\text{fs}} \times (N_\xi + 1)$ equations which can be solved for $\{\mathbf{f}^{(k)}\}_{k=0}^{N_\xi}$. This system of equations is obtained by substituting the operators L_k , D_k , U_k in equation (34) by the $N_{\text{fs}} \times N_{\text{fs}}$ matrices \mathbf{L}_k , \mathbf{D}_k , \mathbf{U}_k , defined in Appendix C. Thus, we discretize (34) as

$$\mathbf{L}_k \mathbf{f}^{(k-1)} + \mathbf{D}_k \mathbf{f}^{(k)} + \mathbf{U}_k \mathbf{f}^{(k+1)} = \mathbf{s}^{(k)}, \quad (51)$$

for $k = 0, 1, \dots, N_\xi$ where $\mathbf{s}^{(k)} \in \mathbb{R}^{N_{\text{fs}}}$ contains $s^{(k)}$ evaluated at the equispaced grid points. Obviously, this system has a block tridiagonal structure and the algorithm presented in subsection 3.1 can be applied to it. We just have to replace in equations (39), (40) and (43) the operators and functions by their respective

matrix and vector analogues, which we denote by boldface letters. The matrix approximation to the forward elimination procedure given by equations (39) and (40) reads

$$\Delta_k = D_k - U_k \Delta_{k+1}^{-1} L_{k+1}, \quad (52)$$

$$\sigma^{(k)} = s^{(k)} - U_k \Delta_{k+1}^{-1} \sigma^{(k+1)}, \quad (53)$$

for $k = N_\xi - 1, N_\xi - 2, \dots, 0$ (in this order). Thus, starting from $\Delta_{N_\xi} = D_{N_\xi}$ and $\sigma^{(N_\xi)} = s^{(N_\xi)}$ all the matrices Δ_k and the vectors $\sigma^{(k)}$ are defined from equations (52) and (53). Obtaining the matrix Δ_k from equation (52) requires to invert Δ_{k+1} , perform two matrix multiplications and a subtraction of matrices. The inversion using LU factorization and each matrix multiplication require $O(N_{\text{fs}}^3)$ operations so it is desirable to reduce the number of matrix multiplications as much as possible. For $k \geq 2$, we can reduce the number of matrix multiplications in determining Δ_k to one if instead of computing Δ_{k+1}^{-1} we solve for X_{k+1} the matrix system of equations

$$\Delta_{k+1} X_{k+1} = L_{k+1}, \quad (54)$$

and then obtain

$$\Delta_k = D_k - U_k X_{k+1}, \quad (55)$$

for $k = N_\xi - 1, N_\xi - 2, \dots, 2$. For $k \leq 1$ as we need to solve (41) and do the backward substitution (43), it is convenient to compute and store Δ_k^{-1} . Besides, as none of the source terms s_1 , s_2 and s_3 given by (19) have Legendre modes greater than 2 we have from equation (53) that $\sigma^{(k)} = 0$ for $k \geq 3$ and $\sigma^{(2)} = s^{(2)}$ and (53) must be applied just when $k = 0$ and $k = 1$. Applying once (53) requires $O(N_{\text{fs}}^2)$ operations and its contribution to the arithmetic complexity of the algorithm is subdominant with respect to the matrix inversions and multiplications. As the resolution of a matrix system of equations and matrix multiplication must be done $N_\xi + 1$ times, solving equation (51) by this method requires $O(N_\xi N_{\text{fs}}^3)$ operations.

In what concerns to memory resources, as we are only interested in the Legendre modes 0, 1 and 2, it is not necessary to store in memory all the matrices L_k , D_k , U_k and Δ_k . Instead, we store solely L_k , U_k and Δ_k^{-1} for $k = 0, 1, 2$. For the intermediate steps we just need to use some auxiliary matrices L , D , U , Δ and X . This makes the amount of memory required by MONKES independent of N_ξ , being of order N_{fs}^2 .

To summarize, the pseudocode of the implementation of the algorithm in MONKES is given in Algorithm 1. In the first loop from $k = N_\xi - 1$ to $k = 2$ we construct L_2 , Δ_2^{-1} and U_2 without saving any matrix from the intermediate steps nor computing any vector $\sigma^{(k)}$. After that, in the second loop from $k = 1$ to $k = 0$, the matrices L_k and Δ_k^{-1} are computed and saved for

Algorithm 1 Block tridiagonal solution algorithm implemented in MONKES.

Forward elimination:

```

L ← LNξ                                ▷ Starting value for L
Δ ← DNξ                                ▷ Starting value for Δ
for k = Nξ − 1 to 2 do
    Solve ΔX = L                        ▷ Compute Xk+1 stored in X
    L ← Lk                                ▷ Construct Lk stored in L
    D ← Dk                                ▷ Construct Dk stored in D
    U ← Uk                                ▷ Construct Uk stored in U
    Δ ← D − UX                        ▷ Construct Δk stored in Δ
    if k = 2 then                            ▷ Save required matrices
        Lk ← L                                ▷ Save L2
        Solve ΔΔk−1 = Identity        ▷ Compute Δ2−1
        Uk ← U                                ▷ Save U2
    end if
end for
for k = 1 to 0 do
    if k > 0 then Lk ← Lk                ▷ Construct and save Lk
    D ← Dk                                ▷ Construct Dk stored in D
    Uk ← Uk                                ▷ Construct and save Uk
    Δk−1 ← D − UkΔk+1−1Lk        ▷ Construct Δk
    σ(k) ← s(k) − UkΔk+1−1σ(k+1)    ▷ Construct σ(k)
    Solve ΔΔk−1 = Identity        ▷ Compute Δk−1
end for

```

Backward substitution:

```

f(0) ← Δ0−1σ(0)
for k = 1 to 2 do
    f(k) ← Δk−1(σ(k) − Lkf(k−1))
end for

```

the posterior step of backward substitution. Once we have solved (51) for $\mathbf{f}^{(0)}$, $\mathbf{f}^{(1)}$ and $\mathbf{f}^{(2)}$, the integrals of the flux-surface average operation involved in the geometric coefficients (44), (45), (46) and (47), are conveniently computed using the trapezoidal rule, which for periodic analytic functions has geometric convergence [39]. In section 3 we will see that despite the cubic scaling in N_{fs} of the arithmetical complexity of the algorithm, it is possible to obtain fast and accurate calculations of the monoenergetic geometric coefficients at low collisionality (in particular \hat{D}_{31}) in a single processor. The reason behind this is that in the asymptotic relation $O(N_{\text{fs}}^3) \sim C_{\text{alg}} N_{\text{fs}}^3$, the constant C_{alg} is small enough to allow N_{fs} to take a sufficiently high value to capture accurately the spatial dependence of the distribution function without increasing much the wall-clock time.

The algorithm is implemented in the new code MONKES, written in Fortran language. The matrix inversions and multiplications are computed using the linear algebra library LAPACK [40].

4. Code performance and benchmark

In this section we will demonstrate how MONKES provides fast and accurate calculations of the monoenergetic coefficients from low ($\hat{\nu} = 10^{-5} \text{ m}^{-1}$) to high collisionality ($\hat{\nu} = 3 \cdot 10^2 \text{ m}^{-1}$).

In subsection 4.1 we will see that the number of points required for a correct calculation of the monoenergetic coefficients for $\hat{\nu} \geq 10^{-5} \text{ m}$ are below $N_{\text{fs}} = 2000$ points and less than $N_{\xi} = 200$ Legendre modes. In subsection 4.2 it is demonstrated that for these resolutions MONKES produces fast calculations in a single processor. Specifically, for the accurate evaluation of monoenergetic coefficients in six cases selected, it will require approximately 1 minute. Finally, in subsection 4.3 the coefficients computed with MONKES will be benchmarked with DKES and, for some cases in which DKES calculations are not accurate, with the code SFINCS. As a result of the benchmarking, we will conclude that MONKES is not only faster, but also more accurate than DKES.

4.1. Convergence of monoenergetic coefficients at low collisionality

In the low collisionality regime, convection is dominant with respect to diffusion. As equation (18) is singularly perturbed with respect to $\hat{\nu}$, its solution possesses internal boundary layers in ξ . These boundary layers appear at the interfaces between different classes of trapped particles. At these regions of phase space, collisions are no longer subdominant with respect to advection. Besides, at these regions, the poloidal $\mathbf{E} \times \mathbf{B}$ precession from equation (18) can produce the chaotic transition of collisionless particles from one class to another due to separatrix crossing mechanisms [41, 24]. The existence of these localized regions with large ξ gradients forces to take a truncated expansion with a high number of Legendre modes N_{ξ} , explaining the difficulty to obtain fast and accurate solutions to equation (18) at low collisionality.

In this subsection we will select resolutions N_{θ} , N_{ζ} and N_{ξ} for which MONKES provides accurate calculations of the monoenergetic coefficients in a wide range of collisionalities. For this, we will study how the monoenergetic coefficients computed by MONKES converge with N_{θ} , N_{ζ} and N_{ξ} at the low collisionality regime. From the point of view of numerical analysis, it is the lack of diffusion along ξ in equation (18) the responsible for the necessity of large values of N_{ξ} . Hence, if MONKES is capable of producing fast and accurate calculations at low collisionality, it will also produce fast and accurate calculations at higher collisionalities.

|| In this context “accurate at high collisionality” means that the drift-kinetic equation (18) is solved accurately.

For the convergence study, we select three different magnetic configurations at a single flux surface. Two of them correspond to configurations of W7-X: EIM and KJM. The third one corresponds to the new QI “flat mirror” [8] configuration CIEMAT-QI [7]. This selection of cases is meant to represent what types of magnetic configurations will need to be evaluated when optimizing QI stellarators. The calculations are done for the $1/\nu$ ($\hat{E}_r = 0$) and $\sqrt{\nu}$ regimes at the low collisionality value $\hat{\nu} = 10^{-5} \text{ m}$. In table 1 the cases considered are enlisted, with their correspondent values of $\hat{E}_r := \hat{E}_{\psi} d\psi/dr$. We have denoted $r = L_a \sqrt{\psi/\psi_{\text{lcs}}}$, where L_a is the minor radius of the device¶.

Configuration	ψ/ψ_{lcs}	$\hat{\nu} [\text{m}^{-1}]$	$\hat{E}_r [\text{kV} \cdot \text{s}/\text{m}^2]$
W7X-EIM	0.200	10^{-5}	0
W7X-EIM	0.200	10^{-5}	$3 \cdot 10^{-4}$
W7X-KJM	0.204	10^{-5}	0
W7X-KJM	0.204	10^{-5}	$3 \cdot 10^{-4}$
CIEMAT-QI	0.250	10^{-5}	0
CIEMAT-QI	0.250	10^{-5}	10^{-3}

Table 1: Cases considered in the convergence study of monoenergetic coefficients and values of $(\hat{\nu}, \hat{E}_r)$.

In order to select the triplets $(N_{\theta}, N_{\zeta}, N_{\xi})$ for “sufficiently accurate” calculations of \hat{D}_{31} , we need to define properly what it means to be “sufficiently converged”. For each case of table 1 we will proceed in the same manner. First, we plot the coefficients \hat{D}_{ij} as functions of the number of Legendre modes in a sufficiently wide interval. For each value of N_{ξ} , the selected spatial resolutions N_{θ} and N_{ζ} are sufficiently large so that increasing them varies the monoenergetic coefficients in less than a 1%. We will say that these calculations are “spatially converged”. As typically the most difficult coefficient to calculate is the bootstrap current coefficient, we will select the resolutions so that \hat{D}_{31} is accurately computed. From the curve of (spatially converged) \hat{D}_{31} as a function of N_{ξ} we define our converged reference value, which we denote by \hat{D}_{31}^r , as the converged calculation to three significant digits. From this converged reference value we will define two regions. A first region

$$\mathcal{R}_{\epsilon} := [(1 - \epsilon/100)\hat{D}_{31}^r, (1 + \epsilon/100)\hat{D}_{31}^r] \quad (56)$$

for calculations that deviate less than or equal to an $\epsilon\%$ with respect to \hat{D}_{31}^r . This interval will be used for selecting the resolutions through the following convergence criteria.

¶ DKES uses r as radial coordinate instead of ψ . The quantities $\hat{\nu}$ and \hat{E}_r are denoted respectively CMUL and EFIELD in the code DKES.

We say that, for fixed $(N_\theta, N_\zeta, N_\xi)$ and ϵ , a calculation $\hat{D}_{31} \in \mathcal{R}_\epsilon$ is sufficiently converged if, two conditions are satisfied

- (i) Spatially converged calculations with $N'_\xi \geq N_\xi$ belong to \mathcal{R}_ϵ .
- (ii) Increasing N_θ and N_ζ while keeping N_ξ constant produces calculations which belong to \mathcal{R}_ϵ .

Condition (i) is used to select the number of Legendre modes N_ξ and condition (ii) is used to select the values of N_θ and N_ζ once N_ξ is fixed.

Additionally, we define a second interval

$$\mathcal{A}_\epsilon := [\hat{D}_{31}^r - \epsilon, \hat{D}_{31}^r + \epsilon] \quad (57)$$

to distinguish which calculations are at a distance less or equal to ϵ of \hat{D}_{31}^r . The reason to have two different regions is that for stellarators close to QI, the relative convergence criteria can become too demanding (the smaller \hat{D}_{31}^r is, the narrower \mathcal{R}_ϵ becomes). Nevertheless, for optimization purposes, it is sufficient to ensure that $|\hat{D}_{31}|$ is sufficiently small⁺. We will use this interval for two purposes: first to give a visual idea of how narrow \mathcal{R}_ϵ becomes. Secondly, to show how in the case in which \mathcal{R}_ϵ is very small, it is easier to satisfy an absolute criteria than a relative one.

Figure 1 shows the convergence of monoenergetic coefficients with the number of Legendre modes for W7-X EIM in the $1/\nu$ regime. From figures 1a and 1b we see that the radial transport and parallel conductivity coefficients converge monotonically with N_ξ . On the other hand, the bootstrap current coefficient is more difficult to converge as can be seen on 1c. As a sanity check, the fulfilment of the Onsager symmetry relation $\hat{D}_{31} = -\hat{D}_{13}$ is included. The converged reference value \hat{D}_{31}^r taken is the spatially converged calculation for $N_\xi = 380$. Defining a region of relative convergence of $\epsilon = 5\%$, allows to select a resolution of $N_\xi = 140$ Legendre modes to satisfy condition (i). The selection is indicated with a five-point green star. Note that for this case, an absolute deviation of 0.005 m from \hat{D}_{31}^r is slightly more demanding than the relative condition. From figure 1d we choose the resolutions $(N_\theta, N_\zeta) = (23, 55)$ to satisfy convergence condition (ii).

The $\sqrt{\nu}$ regime case of W7-X EIM is shown in figure 2. We notice from figure 2c that obtaining sufficiently converged results for the region \mathcal{R}_5 is more difficult than in the $1/\nu$ regime. For this case, the sizes of the intervals $\mathcal{A}_{0.005}$ and \mathcal{R}_5 are almost the same. This is in part due to the fact that the \hat{D}_{31} coefficient is smaller in absolute value and thus, the region \mathcal{R}_5 is

⁺ If we optimize for quasi-isodynamicity using a value $\hat{D}_{31} = \hat{D}_{31}^r + \epsilon \in \mathcal{A}_\epsilon$, and for the optimized stellarator $\hat{D}_{31} = 0$, then it is reasonable to expect that the converged value is consequently small $|\hat{D}_{31}| \sim |\epsilon|$.

narrower. We select $N_\xi = 160$ to satisfy condition (i). The selection $(N_\theta, N_\zeta) = (27, 55)$ satisfies condition (ii) as shown in figure 2d.

The convergence curves for the case of W7-X KJM in the $1/\nu$ regime are shown in figure 3. Due to the smallness of \hat{D}_{31}^r , the amplitude of the region \mathcal{R}_5 is much narrower than in the EIM case, being of order 10^{-3} . It is so narrow that the absolute value region $\mathcal{A}_{0.005}$ contains the relative convergence region. It is shown in figure 3c that taking $N_\xi = 140$ is sufficient to satisfy condition (i). According to the convergence curves plotted in figure 3d, selecting $(N_\theta, N_\zeta) = (23, 63)$ ensures satisfying condition (ii).

The case of W7-X KJM in the $\sqrt{\nu}$ regime is shown in figure 4. The selection of $N_\xi = 180$ Legendre modes, indicated in figure 4c, satisfies convergence condition (i). As shown in figure 4d, condition (ii) is satisfied by the selection $(N_\theta, N_\zeta) = (19, 79)$.

The convergence of monoenergetic coefficients for the nearly quasi-isodynamic configuration CIEMAT-QI in the $1/\nu$ regime is shown in figure 5. Note that as in the W7-X KJM case at this regime, the region of absolute error $\mathcal{A}_{0.005}$ is bigger than the relative one. As the monoenergetic coefficients are smaller, we relax the relative convergence parameter to $\epsilon = 7\%$. In figure 5c we see that the region of 7% of deviation \mathcal{R}_7 is quite narrow and that selecting $N_\xi = 180$ satisfies condition (i). To satisfy condition (ii), we choose the resolutions $(N_\theta, N_\zeta) = (15, 119)$ as shown in figure 5d.

Finally, the case of CIEMAT-QI in the $\sqrt{\nu}$ regime is shown in figure 6. Looking at figure 6c we can check that taking $N_\xi = 180$ satisfies condition (i) for the region \mathcal{R}_7 of 7% of deviation. In this case, the region of absolute error $\mathcal{A}_{0.001}$ is five times smaller than in the rest of cases and is still bigger than the relative error region. As shown in figure 6d, the selection $(N_\theta, N_\zeta) = (15, 119)$ satisfies condition (ii).

4.2. Code performance

In this subsection we will compare MONKES and DKES performance in terms of the wall-clock time and describe MONKES scaling properties. For the wall-clock time comparison, a convergence study (similar to the one explained in subsection 4.1) has been carried out with DKES on Appendix D. This convergence study is done to compare the wall-clock times between MONKES and DKES for the same level of relative convergence with respect to \hat{D}_{31}^r . The comparison is displayed in table 2 along with the minimum number of Legendre modes for which DKES results satisfy convergence condition (i). In all three cases, MONKES is faster than DKES despite using more Legendre modes. Even for W7-X EIM, in which we have taken $N_\xi = 80$ for DKES calculations, MONKES is faster using almost twice the number of Legendre modes. For the high mirror configuration, MONKES is

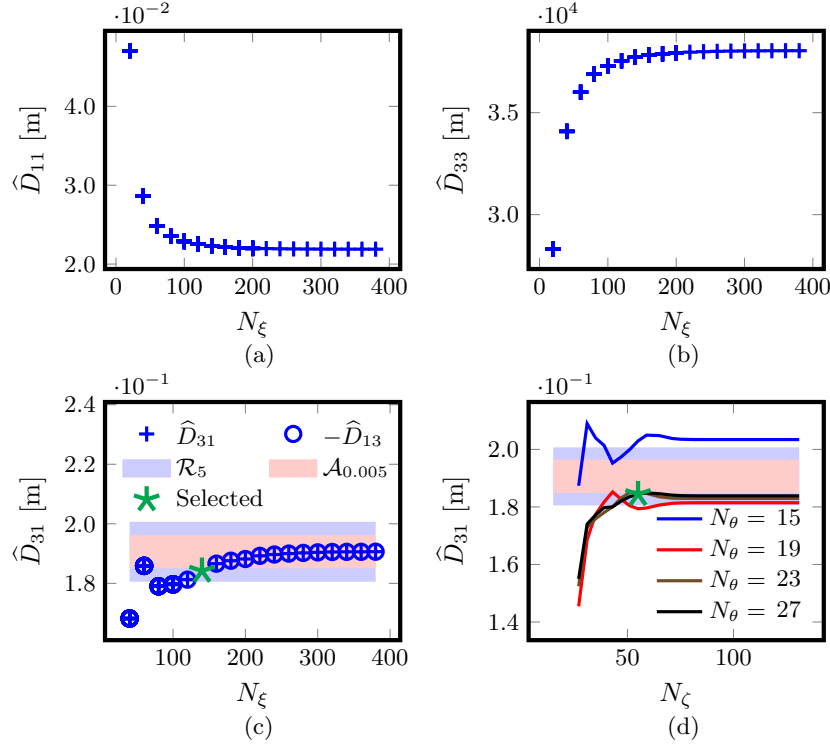


Figure 1: Convergence of monoenergetic coefficients with the number of Legendre modes N_ξ for W7X-EIM at the surface labelled by $\psi/\psi_{\text{lfs}} = 0.200$, for $\hat{\nu}(v) = 10^{-5} \text{ m}^{-1}$ and $\hat{E}_r(v) = 0 \text{ kV} \cdot \text{s/m}^2$.

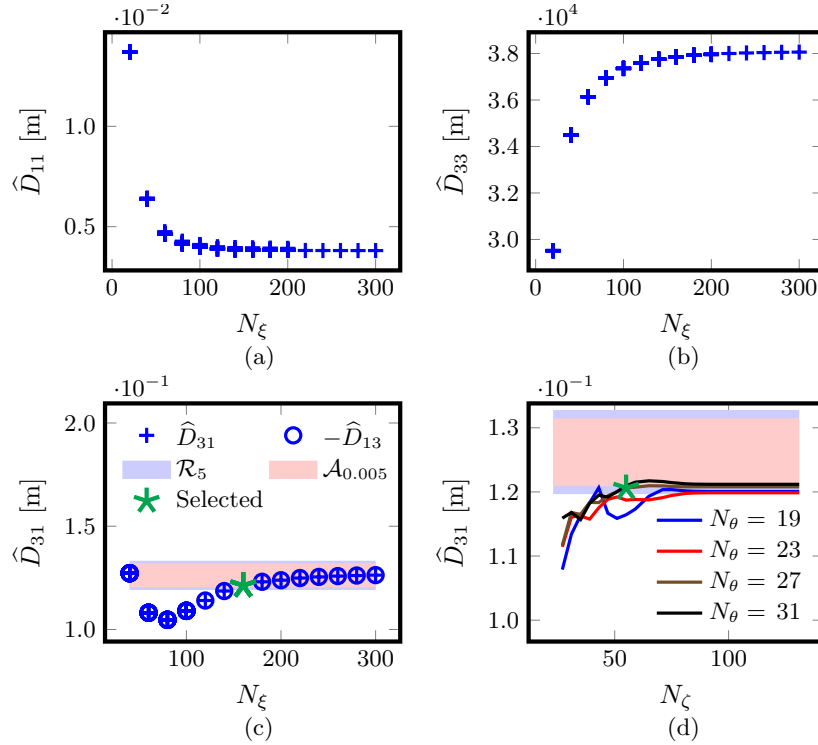


Figure 2: Convergence of monoenergetic coefficients with the number of Legendre modes N_ξ for W7X-EIM at the surface labelled by $\psi/\psi_{\text{lfs}} = 0.200$, for $\hat{\nu}(v) = 10^{-5} \text{ m}^{-1}$ and $\hat{E}_r = 3 \cdot 10^{-4} \text{ kV} \cdot \text{s/m}^2$.

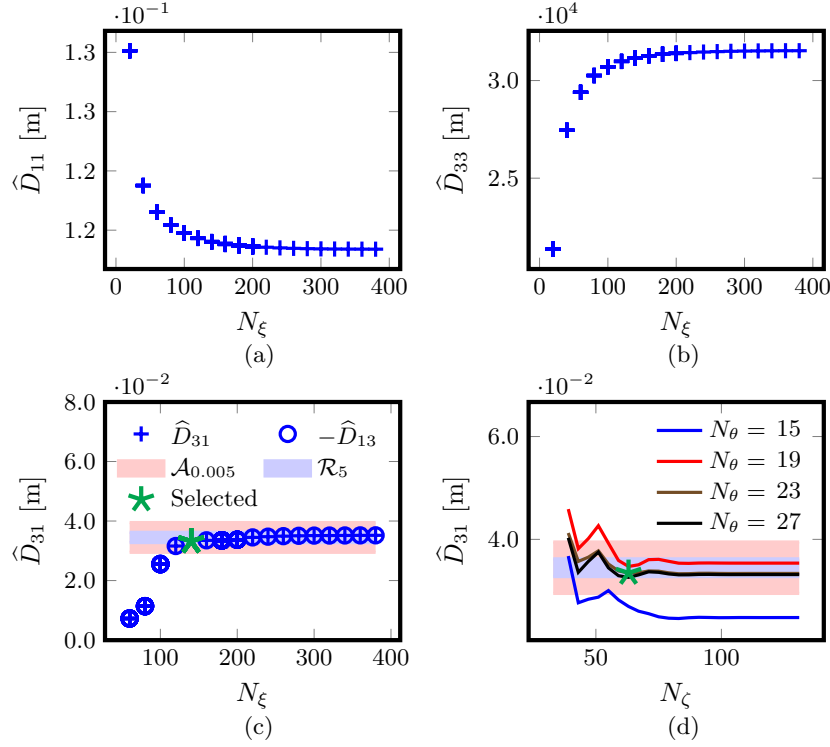


Figure 3: Convergence of monoenergetic coefficients with the number of Legendre modes N_ξ for W7X-KJM at the surface labelled by $\psi/\psi_{\text{lfs}} = 0.204$, for $\hat{v}(v) = 10^{-5} \text{ m}^{-1}$ and $\hat{E}_r(v) = 0 \text{ kV} \cdot \text{s/m}^2$.

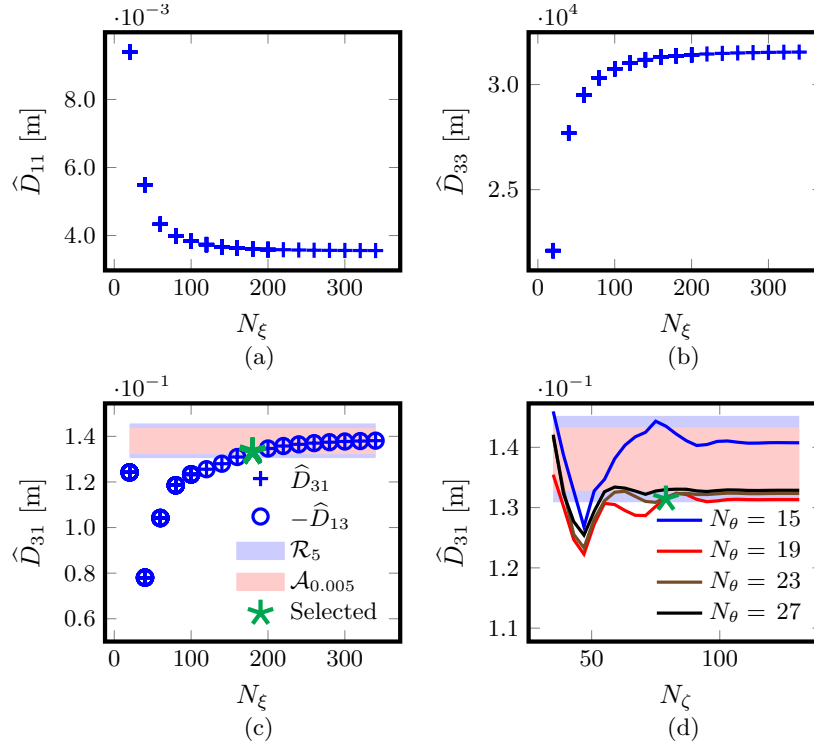


Figure 4: Convergence of monoenergetic coefficients with the number of Legendre modes N_ξ for W7X-KJM at the surface labelled by $\psi/\psi_{\text{lfs}} = 0.204$, for $\hat{v}(v) = 10^{-5} \text{ m}^{-1}$ and $\hat{E}_r(v) = 3 \cdot 10^{-4} \text{ kV} \cdot \text{s/m}^2$.

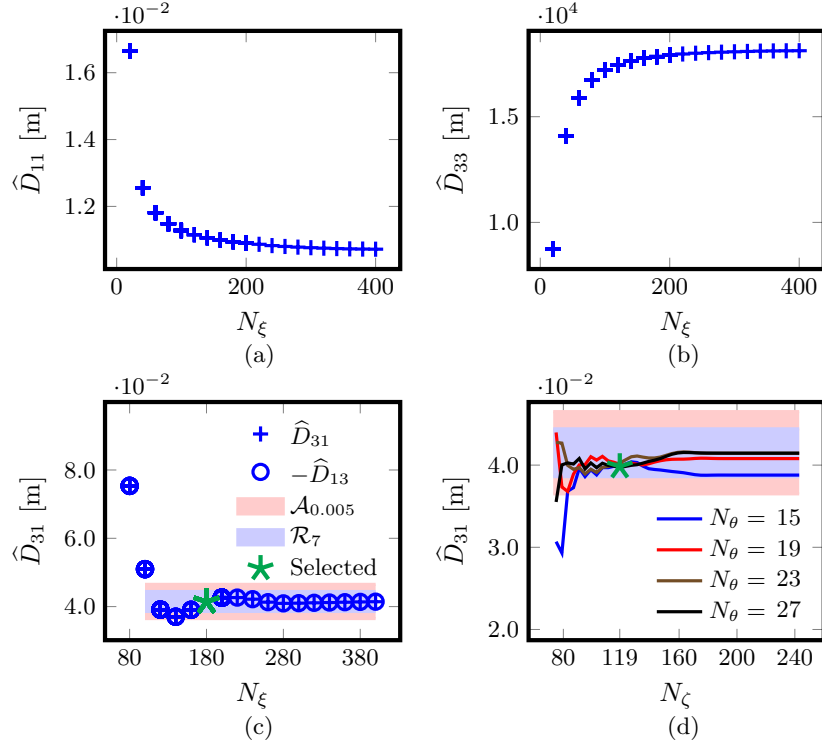


Figure 5: Convergence of monoenergetic coefficients with the number of Legendre modes N_ξ for CIEMAT-QI at the surface labelled by $\psi/\psi_{\text{lfs}} = 0.25$, for $\hat{\nu}(v) = 10^{-5} \text{ m}^{-1}$ and $\hat{E}_r(v) = 0 \text{ kV} \cdot \text{s/m}^2$.

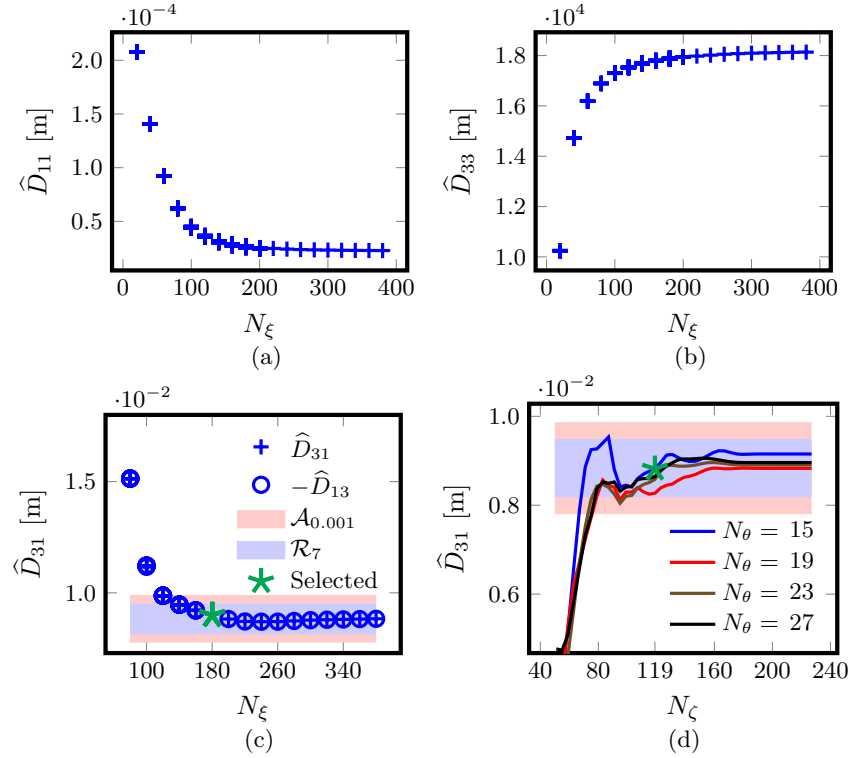


Figure 6: Convergence of monoenergetic coefficients with the number of Legendre modes N_ξ for CIEMAT-QI at the surface labelled by $\psi/\psi_{\text{lfs}} = 0.25$, for $\hat{\nu}(v) = 10^{-5} \text{ m}^{-1}$ and $\hat{E}_r(v) = 10^{-3} \text{ kV} \cdot \text{s/m}^2$.

~ 20 times faster than DKES in the $1/\nu$ regime and ~ 6 times faster than DKES in the $\sqrt{\nu}$ regime. In the case of CIEMAT-QI, MONKES is not only ~ 3 times faster than DKES but we will see in the next subsection that it is also much more accurate.

Case	N_{ξ}^{DKES}	$\epsilon\%$	$t_{\text{clock}}^{\text{DKES}}$ [s]	$t_{\text{clock}}^{\text{MONKES}}$ [s]
W7X-EIM $1/\nu$	80		83.9	22
W7X-EIM $\sqrt{\nu}$	80		57.5	40
W7X-KJM $1/\nu$	120		615	33
W7X-KJM $\sqrt{\nu}$	60		248	46
CIEMAT-QI $1/\nu$	100		238	78
CIEMAT-QI $\sqrt{\nu}$	120		214	78

Table 2: Comparison between the wall-clock time of DKES and MONKES.

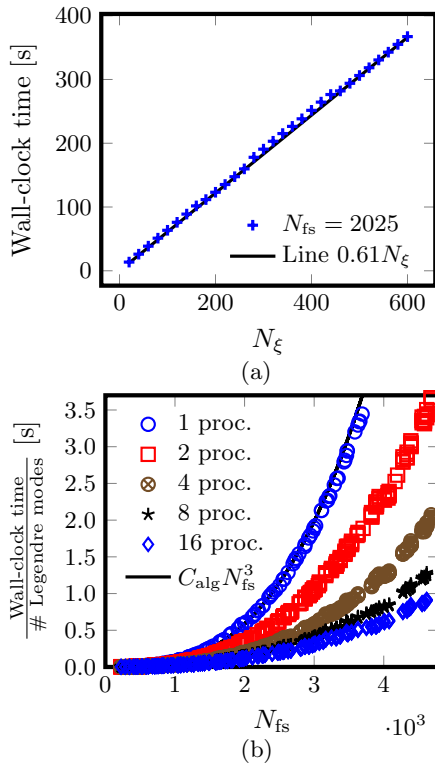


Figure 7: Scaling of MONKES wall-clock time. (a) Linear scaling with the number of Legendre modes for $N_{\text{fs}} = 27 \times 75 = 2025$ discretization points. (b) Cubic scaling with N_{fs} for different number of processors used.

We next check that the arithmetic complexity of the algorithm described in section 3 holds in practice. How MONKES scales with the number of Legendre modes N_{ξ} and the number of points in which the flux surface is discretized is shown in figure 7. To demonstrate the linear scaling, the wall-clock time as a function of N_{ξ} for $N_{\text{fs}} = 2025$ points is represented in figure 7a

and compared with the line of slope 0.61 seconds per Legendre mode. As can be seen in figure 7b, the wall-clock time (per Legendre mode) scales cubically with the number of points in which the flux surface is discretized N_{fs} . As was mentioned at the end of section 3, the constant C_{alg} in a single processor is sufficiently small to give accurate calculations up to $\hat{\nu} \sim 10^{-5} \text{ m}^{-1}$. We have plotted in figure 7b the cubic fit $C_{\text{alg}}N_{\text{fs}}^3$, where $C_{\text{alg}} = 0.61(1/2025)^3 \sim 7 \cdot 10^{-11} \text{ s}$.

As LAPACK library is multithreaded and allows to parallelize the linear algebra operations through several cores, the scaling of MONKES when running in parallel is represented. Additionally, for the resolutions selected in subsection 4.1, we display in table 3 the wall-clock time when running MONKES using several processors in parallel. Note that for the W7-X cases, which require a smaller value of N_{fs} , the speed-up stalls at 8 processors. For CIEMAT-QI, that requires discretizing the flux surface on a finer mesh, this does not happen in the range of processors considered.

Finally, we inform that the wall-clock times for all the calculations shown are those from one of the partitions of CIEMAT's cluster XULA. Specifically, it has been used partition number 2 whose nodes run with Intel Xeon Gold 6254 cores at 3.10 GHz.

Case	No. Processors				
	1	2	4	8	16
W7X-EIM $1/\nu$	22	13	8	5	5
W7X-EIM $\sqrt{\nu}$	40	20	12	8	6
W7X-KJM $1/\nu$	33	17	12	7	7
W7X-KJM $\sqrt{\nu}$	46	17	13	7	7
CIEMAT-QI $1/\nu$	78	45	29	21	16
CIEMAT-QI $\sqrt{\nu}$	78	45	29	21	16

Table 3: Wall-clock time of MONKES in seconds for the selected triplets $(N_{\theta}, N_{\zeta}, N_{\xi})$ when running in several processors.

4.3. Benchmark of the monoenergetic coefficients

Once we have chosen the resolutions $(N_{\theta}, N_{\zeta}, N_{\xi})$ for each case, we need to verify that these selections indeed provide sufficiently accurate calculations of all the monoenergetic coefficients in the interval $\hat{\nu} \in [10^{-5}, 300] \text{ m}^{-1}$. In all cases, MONKES results will be benchmarked against converged calculations from DKES (see Appendix D) and, whenever necessary, from SFINCS*. The benchmarking of the coefficient \hat{D}_{11} is shown in figure 8. For W7-X, perfect agreement for both the $1/\nu$ and $\sqrt{\nu}$ regimes is obtained. This is shown in figures 8a and 8b. For CIEMAT-QI however,

* SFINCS calculations are converged up to 3% in the three independent variables.

it can be seen in figure 8c that DKES fails to predict the $\sqrt{\nu}$ regime that both MONKES and SFINCS capture. The \hat{D}_{11} convergence curve shown in figure D3 of Appendix D reveals that DKES calculation of the \hat{D}_{11} coefficient seems to have converged. Surprisingly, the variational bounds \hat{D}_{11}^{\pm} stall at different values and $|\hat{D}_{11}^{-} - \hat{D}_{11}^{+}|$ does not go to zero with N_{ξ} nor is small compared to \hat{D}_{11} as it should. As both MONKES and SFINCS converge to the same value and DKES does not seem to reduce the error, we conclude that for this case DKES calculations are not accurate.

Figures 9a and 9b show that MONKES calculations of the bootstrap current coefficient for W7-X EIM and W7-X KJM are in total agreement with those of DKES. However, for CIEMAT-QI in both low collisionality regimes, DKES calculation does not converge to a correct value of \hat{D}_{31} . For the $\sqrt{\nu}$ this was expected, as DKES calculation of the \hat{D}_{11} coefficient is not accurate. Surprisingly, in the $1/\nu$ regime, there is agreement between the three codes in the \hat{D}_{11} coefficient and DKES calculation of the \hat{D}_{31} coefficient exceeds the correct calculation by an amount of approximately the 100% of relative error.

For the parallel conductivity coefficient, the results are almost identical for both regimes. We can observe in figure 10 that for all three configurations, the agreement between MONKES and DKES results is almost perfect and the conductivity coefficient approaches the Spitzer one when the collisionality is increased.

5. Conclusions and future work

In this paper we have presented the new code MONKES, which can provide fast and accurate calculations of the monoenergetic transport coefficients at low collisionality in a single processor. Through a thorough convergence study we have shown that is possible to evaluate the monoenergetic coefficients at the $1/\nu$ and $\sqrt{\nu}$ regimes in approximately 1 minute. Besides, when there are sufficient computational resources available, the code can run very fast using several processors in parallel. A natural application for MONKES is to include it in a stellarator optimization suite. MONKES rapid calculations will allow direct optimization of the bootstrap current and radial transport from low collisionality to plateau. Massive evaluation of configurations to study the parametric dependence of \hat{D}_{31} or other coefficients on specific quantities of the magnetic configuration can also be done.

The immediate extension of this work is to implement the aforementioned momentum correction techniques from [36]. As each calculation from MONKES can be executed in a single processor, the scan in ν (i.e. in $\hat{\nu}$) required to perform the integrals of the monoenergetic coefficients is parallelizable. Therefore,

it seems possible for the near future to obtain fast calculations of neoclassical transport with a model collision operator that preserves momentum. With this minor extension, MONKES could also be used for self-consistent optimization of magnetic fields in a similar manner to [16].

Its usage within predictive transport frameworks is also possible for high fidelity simulations. For instance, it could be used complemented with KNOSOS in the following manner: For a given plasma profile, the ambipolar radial electric field can be obtained using KNOSOS. Then, this calculation can be improved using MONKES to account for the $1/\nu$ to plateau transition. After that, for the ambipolar radial electric field, the neoclassical fluxes can be calculated. For this, KNOSOS and MONKES can also work complementarily. The \hat{D}_{11} coefficient at the lowest collisionality values can be calculated with KNOSOS and for higher collisionalities with MONKES. A more ambitious inclusion of MONKES in the transport framework would add a step in which the magnetic geometry is modified by the bootstrap current profile.

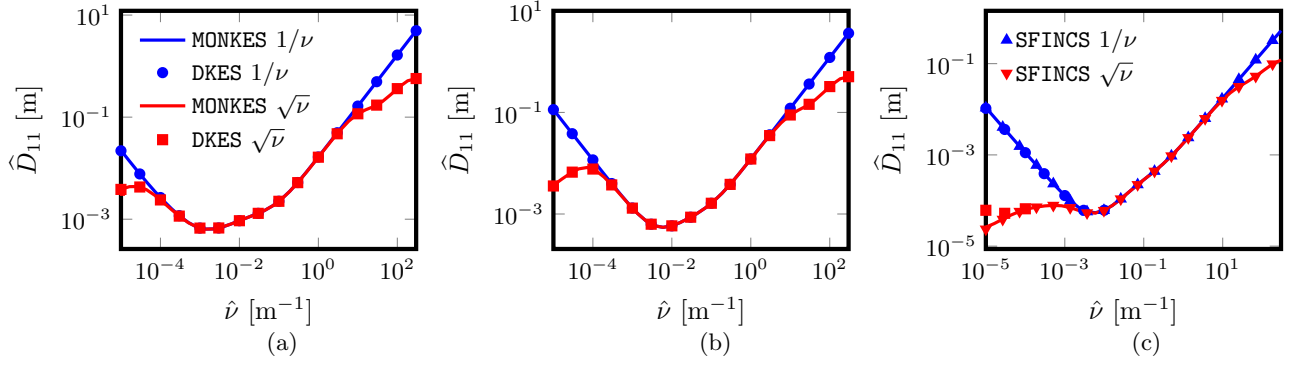


Figure 8: Calculation of \hat{D}_{11} by MONKES and DKES in the $1/\nu$ and $\sqrt{\nu}$ regimes. (a) W7-X EIM at the surface $\psi/\psi_{\text{lcf}_s} = 0.200$. (b) W7-X KJM at the surface $\psi/\psi_{\text{lcf}_s} = 0.204$. (c) CIEMAT-QI at the surface $\psi/\psi_{\text{lcf}_s} = 0.250$.

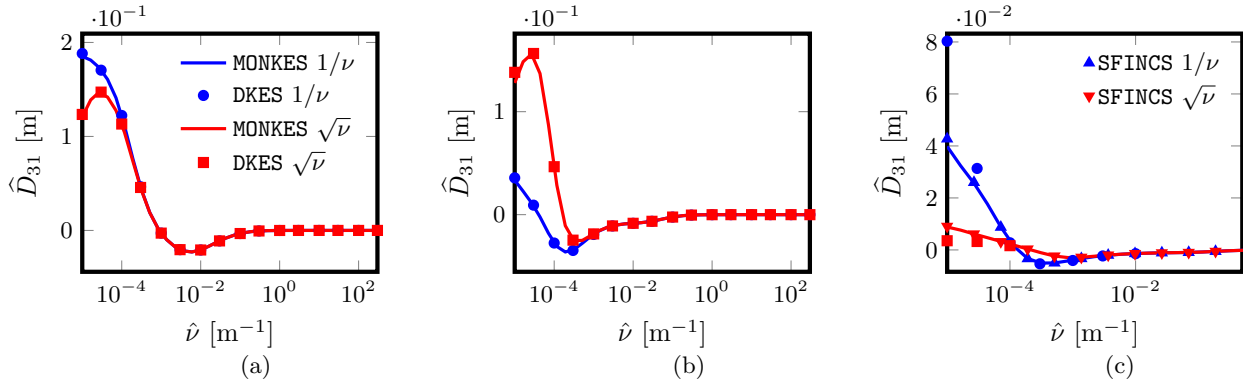


Figure 9: Calculation of \hat{D}_{31} by MONKES and DKES in the $1/\nu$ and $\sqrt{\nu}$ regimes. (a) W7-X EIM at the surface $\psi/\psi_{\text{lcf}_s} = 0.200$. (b) W7-X KJM at the surface $\psi/\psi_{\text{lcf}_s} = 0.204$. (c) CIEMAT-QI at the surface $\psi/\psi_{\text{lcf}_s} = 0.250$.

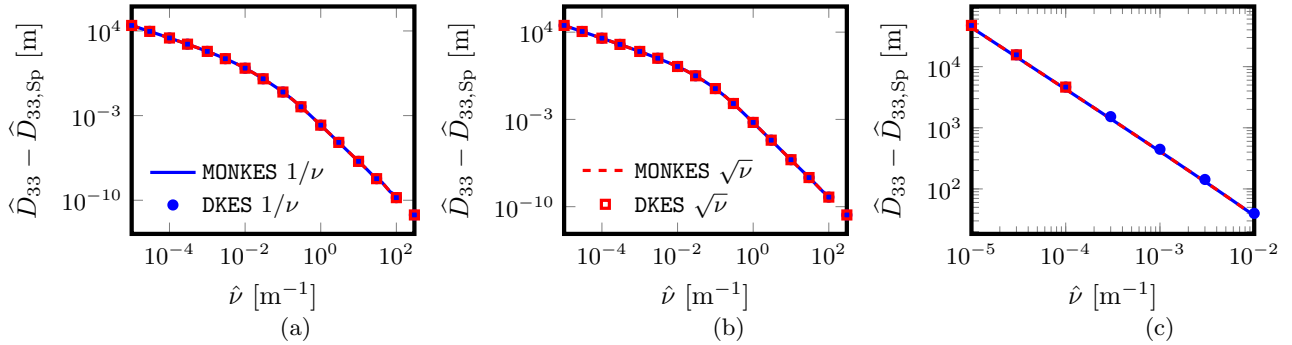


Figure 10: Calculation of \hat{D}_{33} by MONKES and DKES in the $1/\nu$ and $\sqrt{\nu}$ regimes. (a) W7-X EIM at the surface $\psi/\psi_{\text{lcf}_s} = 0.200$. (b) W7-X KJM at the surface $\psi/\psi_{\text{lcf}_s} = 0.204$. (c) CIEMAT-QI at the surface $\psi/\psi_{\text{lcf}_s} = 0.250$.

Appendix A. Legendre modes of the drift-kinetic equation

Legendre polynomials are the eigenfunctions of the Sturm-Liouville problem in the interval $\xi \in [-1, 1]$ defined by the differential equation

$$2\mathcal{L}P_k(\xi) = -k(k+1)P_k(\xi), \quad (\text{A.1})$$

and regularity boundary conditions at $\xi = \pm 1$

$$(1 - \xi^2) \frac{dP_k}{d\xi} \Big|_{\xi=\pm 1} = 0, \quad (\text{A.2})$$

where $k \geq 0$ is an integer.

As \mathcal{L} has a discrete spectrum and is self-adjoint

with respect to the inner product

$$\langle f, g \rangle_{\mathcal{L}} := \int_{-1}^1 f g \, d\xi, \quad (\text{A.3})$$

in the space of functions that satisfy the regularity condition, $\{P_k\}_{k=0}^{\infty}$ is an orthogonal basis satisfying $\langle P_j, P_k \rangle_{\mathcal{L}} = 2\delta_{jk}/(2k+1)$. Hence, these polynomials satisfy the three-term recurrence formula

$$(2k+1)\xi P_k(\xi) = (k+1)P_{k+1}(\xi) + kP_{k-1}(\xi), \quad (\text{A.4})$$

obtained by Gram-Schmidt orthogonalization. Starting the recursion using the initial values $P_0 = 1$ and $P_1 = \xi$ defines the rest of the Legendre polynomials. Additionally, they satisfy the differential identity

$$(1 - \xi^2) \frac{dP_k}{d\xi} = kP_{k-1}(\xi) - k\xi P_k(\xi). \quad (\text{A.5})$$

Identities (A.4) and (A.5) are useful to represent tridiagonally the left-hand side of equation (18) when we use the expansion (33). The k -th Legendre mode of the term $\xi \mathbf{b} \cdot \nabla f$ is expressed in terms of the modes $f^{(k-1)}$ and $f^{(k+1)}$ using (A.4)

$$\langle \xi \mathbf{b} \cdot \nabla f, P_k \rangle_{\mathcal{L}} = \frac{2}{2k+1} \left[\frac{k}{2k-1} \mathbf{b} \cdot \nabla f^{(k-1)} + \frac{k+1}{2k+3} \mathbf{b} \cdot \nabla f^{(k+1)} \right]. \quad (\text{A.6})$$

Combining both (A.4) and (A.5) allows to express the k -th Legendre mode of the mirror term $\nabla \cdot \mathbf{b}((1 - \xi^2)/2) \partial f / \partial \xi$ in terms of the modes $f^{(k-1)}$ and $f^{(k+1)}$ as

$$\left\langle \frac{1}{2}(1 - \xi^2) \nabla \cdot \mathbf{b} \frac{\partial f}{\partial \xi}, P_k \right\rangle_{\mathcal{L}} = \frac{\mathbf{b} \cdot \nabla \ln B}{2k+1} \left[\frac{k(k-1)}{2k-1} f^{(k-1)} - \frac{(k+1)(k+2)}{2k+3} f^{(k+1)} \right], \quad (\text{A.7})$$

where we have also used $\nabla \cdot \mathbf{b} = -\mathbf{b} \cdot \nabla \ln B$. The term proportional to \hat{E}_ψ is diagonal in a Legendre representation

$$\left\langle \frac{\hat{E}_\psi}{\langle B^2 \rangle} \mathbf{B} \times \nabla \psi \cdot \nabla f, P_k \right\rangle_{\mathcal{L}} = \frac{2}{2k+1} \frac{\hat{E}_\psi}{\langle B^2 \rangle} \mathbf{B} \times \nabla \psi \cdot \nabla f^{(k)}. \quad (\text{A.8})$$

For the collision operator used in equation (18), as Legendre polynomials are eigenfunctions of the pitch-angle scattering operator, using (A.1) we obtain the diagonal representation

$$\langle \hat{\nu} \mathcal{L} f, P_k \rangle_{\mathcal{L}} = -\hat{\nu} \frac{k(k+1)}{2k+1} f^{(k)}. \quad (\text{A.9})$$

Finally, we briefly comment on why the truncation error from (33) implies that the solution to (34) and (38) is an approximation of the Legendre spectrum of the exact solution to (18) satisfying (13). For this, we will assume that the solution to (18) and (13) is unique (which it is, see Appendix B). We denote the exact solution by f_{ex} and its Legendre modes by $f_{\text{ex}}^{(k)}$. The Legendre modes $f_{\text{ex}}^{(k)}$ satisfy (34) for all values of k , including $k > N_\xi$ and, in general, $f_{\text{ex}}^{(N_\xi+1)} \neq 0$. Denoting the error of the solution $f^{(k)}$ to (34) and (38) by

$$E^{(k)} := f_{\text{ex}}^{(k)} - f^{(k)}, \quad (\text{A.10})$$

is easy to prove that

$$L_k E^{(k-1)} + D_k E^{(k)} + U_k E^{(k+1)} = 0, \quad (\text{A.11})$$

for $k = 0, 1, \dots, N_\xi - 1$ and

$$L_{N_\xi} E^{(N_\xi-1)} + D_{N_\xi} E^{(N_\xi)} = -U_{N_\xi} f_{\text{ex}}^{(N_\xi+1)}. \quad (\text{A.12})$$

Note that the system of equations constituted by (A.11) and (A.12) for the error is identical to (34) substituting $f^{(k)}$ by $E^{(k)}$ and $s^{(k)}$ by $-U_{N_\xi} f_{\text{ex}}^{(N_\xi+1)}$. Hence, the solution to (A.11) and (A.12) satisfying (38) is unique, implying that $E^{(k)} \neq 0$ unless $U_{N_\xi} f_{\text{ex}}^{(N_\xi+1)} = 0$.

Appendix B. Invertibility of the spatial differential operators

In this Appendix we will study the invertibility of the left-hand-side of (34). For this, we view L_k , D_k and U_k as operators from \mathcal{F} to \mathcal{F} , where \mathcal{F} is the space of smooth functions on the flux-surface equipped with the inner product

$$\langle f, g \rangle_{\mathcal{F}} = \frac{N_p}{4\pi^2} \oint \oint f \bar{g} \, d\theta \, d\zeta, \quad (\text{B.1})$$

where \bar{z} denotes the complex conjugate of z and the induced norm

$$\|f\|_{\mathcal{F}} := \sqrt{\langle f, f \rangle_{\mathcal{F}}}. \quad (\text{B.2})$$

In this setting L_k , D_k and U_k are bounded operators from \mathcal{F} to \mathcal{F} as all of their coefficients are smooth on the flux-surface. However, the operators L_k and U_k given by (35) and (37) do not have a uniquely defined inverse. This is a consequence of the fact that the parallel streaming operator $\xi \mathbf{b} \cdot \nabla + \nabla \cdot \mathbf{b} (1 - \xi^2)/2 \partial / \partial \xi$ has a non trivial kernel comprised of functions $g((1 - \xi^2)/B)$. On the other hand, the operator D_k has a unique inverse for $k \geq 1$.

Whether L_k and U_k are or not invertible can be determined studying the uniqueness of continuous solutions (on the flux-surface) to

$$\mathbf{B} \cdot \nabla f + \omega_k f = sB, \quad (\text{B.3})$$

for some $s \in \mathcal{F}$ and ω_k is a smooth function which is not necessarily univaluated on the torus. Note that equations $L_k f = s$ and $U_k f = s$ can be written in the form of equation (B.3) setting, respectively, $\omega_k = (k-1)\mathbf{B} \cdot \nabla \ln B/2$ and $\omega_k = (k+2)\mathbf{B} \cdot \nabla \ln B/2$. We will determine a condition for ω_k which, if satisfied, equation (B.3) has a unique solution $f \in \mathcal{F}$.

The solution to equation (B.3) can be written as

$$f = (f_0 + K)\Phi, \quad (\text{B.4})$$

where

$$\mathbf{B} \cdot \nabla f_0 = 0, \quad (\text{B.5})$$

$$\mathbf{B} \cdot \nabla \Phi + \omega_k \Phi = 0, \quad (\text{B.6})$$

$$\mathbf{B} \cdot \nabla K = sB/\Phi. \quad (\text{B.7})$$

Equations (B.6) and (B.7) are integrated (along a field line) imposing $\Phi|_p = 1$ and $K|_p = 0$ at a point p of the field line. Note that $f_0 = f|_p$ is an integration constant. Depending on the form of ω_k , f_0 can or cannot be determined imposing continuity on the flux-surface. In order to proceed further, we employ coordinates (α, l) where α is a poloidal angle that labels field lines and l is the length along magnetic field lines, measured from a curve that closes poloidally. Depending on the type of flux-surface there are two possible situations

- (i) For ergodic flux-surfaces, $\iota \in \mathbb{R} \setminus \mathbb{Q}$ and satisfying (B.5) implies that f_0 is a flux function. The solution f to (B.7) is a differentiable function on the torus if $\langle \mathbf{B} \cdot \nabla f \rangle = 0$. Applying (Eq. (B.3)) combined with splitting (B.4) yields

$$\begin{aligned} f_0 \langle \omega_k \Phi \rangle &= \langle Bs \rangle - \langle K \omega_k \Phi \rangle \\ &= \langle \mathbf{B} \cdot \nabla (K\Phi) \rangle. \end{aligned} \quad (\text{B.8})$$

Hence, if $\langle \omega_k \Phi \rangle \neq 0$, equation (B.8) fixes the value of f_0 so that f is continuous on the torus. Note that if $\langle \omega_k \Phi \rangle \neq 0$, by virtue of (B.6), Φ is not univaluated. On the contrary, if f_0 is free, then Φ is a continuous function on the torus.

- (ii) For rational flux-surfaces, $\iota \in \mathbb{Q}$ and satisfying (B.5) implies that $f_0(\alpha)$ depends on the field line chosen. At these surfaces, the field line labelled by α closes on itself after a length $L_c(\alpha)$. If the solution f to is continuous, then $\int_0^{L_c} \mathbf{B} \cdot \nabla f dl/B = 0$. Applying $\int_0^{L_c}$ Eq. (B.3) dl/B

combined with splitting (B.4) yields

$$\begin{aligned} f_0(\alpha) \int_0^{L_c} \omega_k \Phi \frac{dl}{B} &= \int_0^{L_c} s dl - \int_0^{L_c} \omega_k K \Phi \frac{dl}{B} \\ &= \int_0^{L_c} \mathbf{B} \cdot \nabla (K\Phi) \frac{dl}{B}. \end{aligned} \quad (\text{B.9})$$

If $\int_0^{L_c} \omega_k \Phi dl/B \neq 0$, condition (B.9) fixes a unique value of $f_0(\alpha)$ (for each field line) for which f is continuous on the torus. As for ergodic surfaces, continuity of f implies that Φ is multivaluated along field lines.

If (B.8) or (B.9) does not fix f_0 , the operator $\mathbf{B} \cdot \nabla + \omega_k$ from \mathcal{F} to itself is not one to one (it has non trivial kernel comprised of multiples of K). Moreover, when Φ is continuous, (B.8) or (B.9) imposes a condition on the source s . This means that the operator $\mathbf{B} \cdot \nabla + \omega_k$ from \mathcal{F} to itself is not onto. Hence, if $\langle \omega_k \Phi \rangle = 0$ or $\int_0^{L_c} \omega_k \Phi dl/B = 0$, the operator $\mathbf{B} \cdot \nabla + \omega_k$ is not invertible.

This result can be applied to determine that L_k and U_k are not invertible. First, note that the solution to (B.6) can be written as

$$\Phi = \exp(-W_k), \quad (\text{B.10})$$

where $\mathbf{B} \cdot \nabla W_k = \omega_k$ and is integrated imposing $W_k|_p = 0$. For both L_k and U_k , the exponentiated term of Φ takes the form $W_k \propto \ln(B/B|_p)$, which means that $\omega_k \Phi \propto \mathbf{B} \cdot \nabla B$. As B is univaluated we have for L_k and U_k that $\int_0^{L_c} \omega_k \Phi dl/B = 0$ or $\langle \omega_k \Phi \rangle = 0$, which means that neither L_k nor U_k are invertible.

Now we turn our attention to the invertibility of D_k for $k \geq 1$. For $E_\psi = 0$, D_k is just a multiplicative operator and is clearly invertible when $\hat{\nu}, k \neq 0$. For $E_\psi \neq 0$, the invertibility of D_k can be proven by studying the uniqueness of solutions to

$$\mathbf{B} \times \nabla \psi \cdot \nabla g - \hat{\nu}_k g = -\frac{\langle B^2 \rangle}{E_\psi} s, \quad (\text{B.11})$$

where $\hat{\nu}_k = \hat{\nu} k(k+1) \langle B^2 \rangle / 2E_\psi$. The procedure is very similar to the one carried out for L_k and U_k . First, we write the solution to equation (B.11) as

$$g = (g_0 + I)\Psi, \quad (\text{B.12})$$

where

$$\mathbf{B} \times \nabla \psi \cdot \nabla g_0 = 0, \quad (\text{B.13})$$

$$\mathbf{B} \times \nabla \psi \cdot \nabla \Psi - \hat{\nu}_k \Psi = 0, \quad (\text{B.14})$$

$$\mathbf{B} \times \nabla \psi \cdot \nabla I = -\frac{\langle B^2 \rangle}{E_\psi} \frac{s}{\Psi}. \quad (\text{B.15})$$

Equations (B.6) and (B.7) are integrated along a integral curve of $\mathbf{B} \times \nabla \psi$ imposing $\Phi|_p = 1$ and

$I|_p = 0$ at the initial point p of integration. The integral curves of $\mathbf{B} \times \nabla\psi$ are, in Boozer coordinates, straight lines $B_\zeta\theta - B_\theta\zeta = \text{constant}$. In order to proceed further, we change from Boozer angles (θ, ζ) to a different set of magnetic coordinates (α, φ) using the linear transformation

$$\begin{bmatrix} \theta \\ \zeta \end{bmatrix} = \begin{bmatrix} (1 + \iota\delta)^{-1} & \iota \\ -\delta(1 + \iota\delta)^{-1} & 1 \end{bmatrix} \begin{bmatrix} \alpha \\ \varphi \end{bmatrix} \quad (\text{B.16})$$

where $\delta = B_\theta/B_\zeta$. In these coordinates $\mathbf{B} = \nabla\psi \times \nabla\alpha = B_\psi\nabla\psi + B_\varphi\nabla\varphi$ and

$$\mathbf{B} \times \nabla\psi \cdot \nabla = B^2 \frac{\partial}{\partial\alpha}. \quad (\text{B.17})$$

Depending on the rationality or irrationality of δ we can distinguish two options

- (i) If $\delta \in \mathbb{R} \setminus \mathbb{Q}$, satisfying (B.13) implies that g_0 is a flux function (the integral curves trace out the whole flux surface). Note that if g is a differentiable function on the torus $\langle \mathbf{B} \times \nabla\psi \cdot \nabla g \rangle = \langle \nabla \times (g\mathbf{B}) \cdot \nabla\psi \rangle = 0$, where we have used $\nabla \times \mathbf{B} \cdot \nabla\psi = 0$. Taking (Eq. (B.11)) assuming that f is continuous on the flux-surface, combined with (B.12) gives

$$\begin{aligned} \langle \Psi \rangle g_0 &= \frac{\langle B^2 \rangle}{\hat{\nu}_k E_\psi} \langle s \rangle - \langle I\Psi \rangle \\ &= \frac{1}{\hat{\nu}_k} \langle \mathbf{B} \times \nabla\psi \cdot \nabla(I\Psi) \rangle. \end{aligned} \quad (\text{B.18})$$

Hence, if $\langle \Psi \rangle \neq 0$, continuity of g on the torus fixes the integration constant g_0 .

- (ii) If $\delta \in \mathbb{Q}$, satisfying (B.13) implies that $g_0(\varphi)$ is a function of φ . Now the integral curves $\varphi = \text{constant}$ close on itself after moving in α an arc-length L_α . In this scenario, if g is a differentiable function on the torus $\int_0^{L_\alpha} \mathbf{B} \times \nabla\psi \cdot \nabla g \, d\alpha / B^2 = 0$, where we have used (B.17). Thus, taking $\int_0^{L_\alpha} \text{Eq. (B.11)} \, d\alpha / B^2 = 0$, combined with (B.12) gives

$$\begin{aligned} g_0(\varphi) \int_0^{L_\alpha} \Psi \frac{d\alpha}{B^2} &= \frac{\langle B^2 \rangle}{\hat{\nu}_k E_\psi} \int_0^{L_\alpha} s \frac{d\alpha}{B^2} - \int_0^{L_\alpha} I\Psi \frac{d\alpha}{B^2} \\ &= \frac{1}{\hat{\nu}_k} \int_0^{L_\alpha} \mathbf{B} \times \nabla\psi \cdot \nabla(I\Psi) \frac{d\alpha}{B^2}. \end{aligned} \quad (\text{B.19})$$

Thus, if $\int_0^{L_\alpha} \Psi \, d\alpha / B^2 \neq 0$ condition (B.19) fixes the value of $g_0(\varphi)$ so that g is continuous on the flux-surface.

Similarly to what happened to Φ when studying the invertibility of L_k and U_k , continuity of the solution

implies that Ψ cannot be univaluated. We can write Ψ as

$$\Psi = \exp(-A_k), \quad (\text{B.20})$$

where $\mathbf{B} \times \nabla\psi \cdot \nabla A_k = \hat{\nu}_k$ and is integrated along with condition $A_k|_p = 0$. Using (B.17), we can write

$$A_k(\alpha, \varphi) = \hat{\nu}_k \int_0^\alpha \frac{d\alpha'}{B^2(\alpha', \varphi)}. \quad (\text{B.21})$$

Note that A_k is monotonically crescent with α , which means that Ψ cannot be univaluated. Besides, (B.20) implies $\Psi > 0$, which means that $\langle \Psi \rangle \neq 0$ and $\int_0^{L_\alpha} \Psi \, d\alpha / B^2 \neq 0$. Thus, there is a unique value of the constant g_0 which compensates the jumps in Ψ and $I\Psi$ so that $g = g_0\Psi + I\Psi$ is continuous on the flux-surface. Hence, D_k is an invertible operator from \mathcal{F} to itself.

The inverse of D_k for $k \geq 1$ and $E_\psi \neq 0$ is defined by

$$D_k^{-1} := (\mathcal{G}_0[s] + \mathcal{I}[s])\Psi, \quad (\text{B.22})$$

where we have denoted by $\mathcal{G}_0[s]$ and $\mathcal{I}[s]$ to the linear operators which define, respectively, the constant of integration and the solution to (B.15) with $I|_p = 0$ for a given source term. Specifically,

$$\mathcal{I}[s](\alpha, \varphi) := \int_0^\alpha \frac{s(\alpha', \varphi)}{\Psi(\alpha', \varphi)} \frac{d\alpha'}{B^2(\alpha', \varphi)}, \quad (\text{B.23})$$

and

$$\mathcal{G}_0[s](\varphi) := \begin{cases} \text{If } \delta \in \mathbb{R} \setminus \mathbb{Q} : \\ \frac{2}{\hat{\nu}_k(k+1)} \frac{\langle s \rangle}{\langle \Psi \rangle} - \frac{\langle \mathcal{I}[s]\Psi \rangle}{\langle \Psi \rangle}, \\ \text{If } \delta \in \mathbb{Q} : \\ \frac{2}{\hat{\nu}_k(k+1)} \frac{\int_0^{L_\alpha} s \frac{d\alpha}{B^2}}{\int_0^{L_\alpha} \Psi \frac{d\alpha}{B^2}} - \frac{\int_0^{L_\alpha} \mathcal{I}[s]\Psi \frac{d\alpha}{B^2}}{\int_0^{L_\alpha} \Psi \frac{d\alpha}{B^2}}. \end{cases} \quad (\text{B.24})$$

Finally, we will study the invertibility of the operator Δ_k

$$\Delta_k = D_k - U_k \Delta_{k+1}^{-1} L_{k+1} \quad (\text{B.25})$$

assuming that Δ_{k+1} is bounded and invertible. For this, first, we note that in the space of functions of interest (smooth periodic functions on the torus), using a Fourier basis $\{e^{i(m\theta + nN_p\zeta)}\}_{m,n \in \mathbb{Z}}$, we can approximate any function $f(\theta, \zeta) = \sum_{m,n \in \mathbb{Z}} \hat{f}_{mn} e^{i(m\theta + nN_p\zeta)} \in \mathcal{F}$ using an approximant $\tilde{f}(\theta, \zeta)$

$$\tilde{f}(\theta, \zeta) = \sum_{-N \leq m, n \leq N} \hat{f}_{mn} e^{i(m\theta + nN_p\zeta)} \quad (\text{B.26})$$

truncating the modes with mode number greater than some positive integer N where

$$\hat{f}_{mn} = \left\langle f, e^{i(m\theta + nN_p\zeta)} \right\rangle_{\mathcal{F}} \left\| e^{i(m\theta + nN_p\zeta)} \right\|_{\mathcal{F}}^{-2} \quad (\text{B.27})$$

are the Fourier modes of f . Thus, we approximate \mathcal{F} using a finite dimensional subspace $\mathcal{F}^N \subset \mathcal{F}$ consisting on all the functions of the form given by equation (B.26).

Hence, as they are bounded operators, we can approximate D_k , U_k , Δ_{k+1} and L_{k+1} restricted to \mathcal{F}^N (and therefore Δ_k) in equation (B.25) by operators D_k^N , U_k^N , Δ_{k+1}^N and L_{k+1}^N that map any $\tilde{f} \in \mathcal{F}^N$ to the projections of $D_k \tilde{f}$, $U_k \tilde{f}$, $\Delta_{k+1} \tilde{f}$ and $L_{k+1} \tilde{f}$ onto \mathcal{F}^N . The operators D_k^N , U_k^N , Δ_{k+1}^N and L_{k+1}^N can be exactly represented (in a Fourier basis) by square matrices of size $\dim \mathcal{F}^N$. When the operators are invertible, these matrices are invertible aswell. Doing so, we can interpret the matrix representation of Δ_k as the Schur complement of the matrix

$$M_k^N = \begin{bmatrix} D_k^N & U_k^N \\ L_{k+1}^N & \Delta_{k+1}^N \end{bmatrix}. \quad (\text{B.28})$$

It is well known from linear algebra that the Schur complement of M_k^N is invertible when both D_k^N and Δ_{k+1}^N are (which they are). Hence, for $k \geq 1$, the matrix Δ_k^N can be inverted for any N , and therefore Δ_k is invertible. For $k = 0$, it is necessary to substitute one of the rows of $[D_k^N \ U_k^N]$ by the condition (38) so that M_k^N is invertible for any N and as Δ_1^N can be inverted, also Δ_0^N constructed in this manner for any N , which implies that Δ_0 is invertible.

Appendix C. Fourier collocation method

In this appendix we describe the Fourier collocation (also called pseudospectral) method for discretizing the angles θ and ζ . This discretization will be used to obtain the matrices \mathbf{L}_k , \mathbf{D}_k and \mathbf{U}_k . For convenience, we will use the complex version of the discretization method but for the discretization matrices we will just take their real part as the solutions to (18) are all real. We search for approximate solutions to equation (34) of the form

$$f^{(k)}(\theta, \zeta) = \sum_{n=-N_{\zeta 1}/2}^{N_{\zeta 2}/2-1} \sum_{m=-N_{\theta 1}/2}^{N_{\theta 2}/2-1} \tilde{f}_{mn}^{(k)} e^{i(m\theta + nN_p\zeta)} \quad (\text{C.1})$$

where $N_{\theta 1} = N_{\theta} - N_{\theta} \bmod 2$, $N_{\theta 2} = N_{\theta} + N_{\theta} \bmod 2$, $N_{\zeta 1} = N_{\zeta} - N_{\zeta} \bmod 2$, $N_{\zeta 2} = N_{\zeta} + N_{\zeta} \bmod 2$ for some positive integers N_{θ} , N_{ζ} . The complex numbers

$$\tilde{f}_{mn}^{(k)} := \left\langle f^{(k)}, e^{i(m\theta + nN_p\zeta)} \right\rangle_{N_{\theta}N_{\zeta}} \left\| e^{i(m\theta + nN_p\zeta)} \right\|_{N_{\theta}N_{\zeta}}^{-2} \quad (\text{C.2})$$

are the discrete Fourier modes (also called discrete Fourier transform),

$$\langle f, g \rangle_{N_{\theta}N_{\zeta}} := \frac{1}{N_{\theta}N_{\zeta}} \sum_{j'=0}^{N_{\zeta}-1} \sum_{i'=0}^{N_{\theta}-1} f(\theta_{i'}, \zeta_{j'}) \overline{g(\theta_{i'}, \zeta_{j'})} \quad (\text{C.3})$$

is the discrete inner product associated to the equispaced grid points (49), (50), $\|f\|_{N_{\theta}N_{\zeta}} := \sqrt{\langle f, f \rangle_{N_{\theta}N_{\zeta}}}$ its induced norm and \bar{z} denotes the complex conjugate of z . We denote by $\mathcal{F}^{N_{\theta}N_{\zeta}}$ to the finite dimensional vector space (of dimension $N_{\theta}N_{\zeta}$) comprising all the functions that can be written in the form of expansion (C.1).

The set of functions $\{e^{i(m\theta + nN_p\zeta)}\} \subset \mathcal{F}^{N_{\theta}N_{\zeta}}$ forms an orthogonal basis for $\mathcal{F}^{N_{\theta}N_{\zeta}}$ equipped with the discrete inner product (C.3). Namely,

$$\left\langle e^{i(m\theta + nN_p\zeta)}, e^{i(m'\theta + n'N_p\zeta)} \right\rangle_{N_{\theta}N_{\zeta}} \propto \delta_{mm'} \delta_{nn'} \quad (\text{C.4})$$

for $-N_{\theta 1}/2 \leq m \leq N_{\theta 2}/2$ and $-N_{\zeta 1}/2 \leq n \leq N_{\zeta 2}/2$. Thus, for functions lying in $\mathcal{F}^{N_{\theta}N_{\zeta}}$, discrete expansions such as (C.1) coincide with their (finite) Fourier series. The discrete Fourier modes (C.2) are chosen so that the expansion (C.1) interpolates $f^{(k)}$ at grid points. Hence, there is a vector space isomorphism between the space of discrete Fourier modes and $f^{(k)}$ evaluated at the equispaced grid.

Combining equations (C.1), (C.2) and (C.3) we can write our Fourier interpolant as

$$\begin{aligned} f^{(k)}(\theta, \zeta) &= \mathbf{I}(\theta, \zeta) \cdot \mathbf{f}^{(k)} \\ &= \sum_{j'=0}^{N_{\zeta}-1} \sum_{i'=0}^{N_{\theta}-1} I_{i'j'}(\theta, \zeta) f^{(k)}(\theta_{i'}, \zeta_{j'}), \end{aligned} \quad (\text{C.5})$$

where $\mathbf{f}^{(k)} \in \mathbb{R}^{N_{\text{fs}}}$ is the state vector containing $f^{(k)}(\theta_{i'}, \zeta_{j'})$. The entries of the vector $\mathbf{I}(\theta, \zeta)$ are the functions $I_{i'j'}(\theta, \zeta)$ given by,

$$I_{i'j'}(\theta, \zeta) = I_{i'}^{\theta}(\theta) I_{j'}^{\zeta}(\zeta), \quad (\text{C.6})$$

$$I_{i'}^{\theta}(\theta) = \frac{1}{N_{\theta}} \sum_{m=-N_{\theta 1}/2}^{N_{\theta 2}/2-1} e^{im(\theta - \theta_{i'})}, \quad (\text{C.7})$$

$$I_{j'}^{\zeta}(\zeta) = \frac{1}{N_{\zeta}} \sum_{n=-N_{\zeta 1}/2}^{N_{\zeta 2}/2-1} e^{N_p in(\zeta - \zeta_{j'})}. \quad (\text{C.8})$$

Note that the interpolant is the only function in $\mathcal{F}^{N_{\theta}N_{\zeta}}$ which interpolates the data at the grid points, as $I_{i'}^{\theta}(\theta_i) = \delta_{ii'}$ and $I_{j'}^{\zeta}(\zeta_j) = \delta_{jj'}$.

Of course, our approximation (C.5) cannot (in general) be a solution to (34) at all points $(\theta, \zeta) \in [0, 2\pi) \times [0, 2\pi/N_p)$. Instead, we will force that the

interpolant (C.5) solves equation (34) exactly at the equispaced grid points. Thanks to the vector space isomorphism (C.2) between $\mathbf{f}^{(k)}$ and the discrete modes $\tilde{f}_{mn}^{(k)}$ this is equivalent to match the discrete Fourier modes of the left and right-hand-sides of equation (34).

Inserting the interpolant (C.5) in the left-hand side of equation (34) and evaluating the result at grid points gives

$$\begin{aligned} & \left(L_k \mathbf{f}^{(k-1)} + D_k \mathbf{f}^{(k)} + U_k \mathbf{f}^{(k+1)} \right) \Big|_{(\theta_i, \zeta_j)} = \\ & \left(L_k \mathbf{I} \cdot \mathbf{f}^{(k-1)} + D_k \mathbf{I} \cdot \mathbf{f}^{(k)} + U_k \mathbf{I} \cdot \mathbf{f}^{(k+1)} \right) \Big|_{(\theta_i, \zeta_j)}. \end{aligned} \quad (\text{C.9})$$

Here, $L_k \mathbf{I}(\theta_i, \zeta_j)$, $D_k \mathbf{I}(\theta_i, \zeta_j)$ and $U_k \mathbf{I}(\theta_i, \zeta_j)$ are respectively the rows of \mathbf{L}_k , \mathbf{D}_k and \mathbf{U}_k associated to the grid point (θ_i, ζ_j) . We can relate them to the actual positions they will occupy in the matrices choosing an ordonation of rows and columns. If we use the ordonation that relates respectively the row i_r and column i_c to the grid points (θ_i, ζ_j) and $(\theta_{i'}, \zeta_{j'})$ as

$$i_r = 1 + i + j N_\theta, \quad (\text{C.10})$$

$$i_c = 1 + i' + j' N_\theta, \quad (\text{C.11})$$

for $i, i' = 0, 1, \dots, N_\theta - 1$ and $j, j' = 0, 1, \dots, N_\zeta - 1$. With this ordonation, we define the elements of the row i_r and column i_c given by (C.10) and (C.11) of the matrices \mathbf{L}_k , \mathbf{D}_k and \mathbf{U}_k to be

$$(\mathbf{L}_k)_{i_r i_c} = L_k I_{i' j'}(\theta_i, \zeta_j), \quad (\text{C.12})$$

$$(\mathbf{D}_k)_{i_r i_c} = D_k I_{i' j'}(\theta_i, \zeta_j), \quad (\text{C.13})$$

$$(\mathbf{U}_k)_{i_r i_c} = U_k I_{i' j'}(\theta_i, \zeta_j). \quad (\text{C.14})$$

Explicitly,

$$\begin{aligned} L_k I_{i' j'} \Big|_{(\theta_i, \zeta_j)} &= \frac{k}{2k-1} \left(\mathbf{b} \cdot \nabla I_{i' j'} \Big|_{(\theta_i, \zeta_j)} \right. \\ & \quad \left. + \frac{k-1}{2} \mathbf{b} \cdot \nabla \ln B \Big|_{(\theta_i, \zeta_j)} \delta_{ii'} \delta_{jj'} \right), \end{aligned} \quad (\text{C.15})$$

$$\begin{aligned} D_k I_{i' j'} \Big|_{(\theta_i, \zeta_j)} &= \frac{\hat{E}_\psi}{\langle B^2 \rangle} \mathbf{B} \times \nabla \psi \cdot \nabla I_{i' j'} \Big|_{(\theta_i, \zeta_j)} \\ & \quad + \frac{k(k+1)}{2} \hat{\nu} \delta_{ii'} \delta_{jj'}, \end{aligned} \quad (\text{C.16})$$

$$\begin{aligned} U_k I_{i' j'} \Big|_{(\theta_i, \zeta_j)} &= \frac{k+1}{2k+3} \left(\mathbf{b} \cdot \nabla I_{i' j'} \Big|_{(\theta_i, \zeta_j)} \right. \\ & \quad \left. + \frac{k+2}{2} \mathbf{b} \cdot \nabla \ln B \Big|_{(\theta_i, \zeta_j)} \delta_{ii'} \delta_{jj'} \right), \end{aligned} \quad (\text{C.17})$$

where we have used expressions (31) and (32) to write

$$\begin{aligned} \mathbf{b} \cdot \nabla I_{i' j'} \Big|_{(\theta_i, \zeta_j)} &= \frac{B}{B_\zeta + \iota B_\theta} \Big|_{(\theta_i, \zeta_j)} \\ & \times \left(\iota \delta_{jj'} \frac{dI_{i'}^\theta}{d\theta} \Big|_{\theta_i} - \delta_{ii'} \frac{dI_{j'}^\zeta}{d\zeta} \Big|_{\zeta_j} \right) \end{aligned} \quad (\text{C.18})$$

$$\begin{aligned} \mathbf{B} \times \nabla \psi \cdot \nabla I_{i' j'} \Big|_{(\theta_i, \zeta_j)} &= \frac{B^2}{B_\zeta + \iota B_\theta} \Big|_{(\theta_i, \zeta_j)} \\ & \times \left(B_\zeta \delta_{jj'} \frac{dI_{i'}^\theta}{d\theta} \Big|_{\theta_i} - B_\theta \delta_{ii'} \frac{dI_{j'}^\zeta}{d\zeta} \Big|_{\zeta_j} \right) \end{aligned} \quad (\text{C.19})$$

We remark in first place that, for $k = 0$, the rows of \mathbf{D}_0 and \mathbf{U}_0 associated to the grid point $(\theta_0, \zeta_0) = (0, 0)$, are replaced by equation (38). Finally, each state vector $\mathbf{f}^{(k)}$ for the Fourier interpolants contains the images $f^{(k)}(\theta_{i'}, \zeta_{j'})$ at the grid points, ordered according to (C.11).

Appendix D. Convergence of monoenergetic coefficients calculated by DKES

The code DKES gives an approximation to the monoenergetic geometric coefficients as a semisum of two quantities \hat{D}_{ij}^- and \hat{D}_{ij}^+ by solving a variational principle [30]. For each coefficient, the output of DKES consists on two quantities $\hat{D}_{ij}^\pm K_{ij}$, where K_{ij} are the normalization factors

$$K_{ij} := \left(\frac{d\psi}{dr} \right)^{-2}, \quad i, j \in \{1, 2\}, \quad (\text{D.1})$$

$$K_{i3} := \left(\frac{d\psi}{dr} \right)^{-1}, \quad i \in \{1, 2\}, \quad (\text{D.2})$$

$$K_{3j} := \left(\frac{d\psi}{dr} \right)^{-1}, \quad j \in \{1, 2\}, \quad (\text{D.3})$$

$$K_{33} := 1, \quad (\text{D.4})$$

to change from the radial coordinate ψ to r .

Apart from the normalization factors, there is still a nuance left for the parallel conductivity coefficient: the code DKES computes this coefficient measured with respect to the one obtained by solving the Spitzer problem

$$-\hat{\nu} \mathcal{L} f_{\text{Sp}} = s_3. \quad (\text{D.5})$$

Using (A.1) is immediate to obtain the 1-th Legendre mode of f_{Sp}

$$f_{\text{Sp}}^{(1)} = \frac{1}{\hat{\nu}} \frac{B}{B_0} \quad (\text{D.6})$$

and using (47) we obtain its associated \hat{D}_{33} coefficient

$$\hat{D}_{33, \text{Sp}} = \frac{2}{3\hat{\nu}} \left\langle \frac{B^2}{B_0^2} \right\rangle. \quad (\text{D.7})$$

Thus, the output of DKES for the parallel conductivity coefficient has to be compared against the deviation $(\hat{D}_{33} - \hat{D}_{33,\text{Sp}})$.

From the output of DKES, the diagonal elements \hat{D}_{ii}^\pm satisfy $\hat{D}_{ii}^- \geq \hat{D}_{ii} \geq \hat{D}_{ii}^+$ and allow to compute bounds for \hat{D}_{ij}

$$\frac{\hat{D}_{ij}^- + \hat{D}_{ij}^+}{2} - \Delta_{ij} \leq \hat{D}_{ij} \leq \frac{\hat{D}_{ij}^- + \hat{D}_{ij}^+}{2} + \Delta_{ij} \quad (\text{D.8})$$

and $\Delta_{ij} = \sqrt{(\hat{D}_{ii}^- - \hat{D}_{ii}^+)(\hat{D}_{jj}^- - \hat{D}_{jj}^+)}/2$.

In figures D1, D2 and D3, the convergence with the number of Legendre modes of the monoenergetic coefficients calculated by DKES is shown. Additionally, on figures D1b, D1e, D2b, D2e, D3b and D3e we plot the regions of convergence \mathcal{R}_ϵ for each case. Due to the extremely large values of Δ_{31} , the variational bounds for \hat{D}_{31} have been omitted.

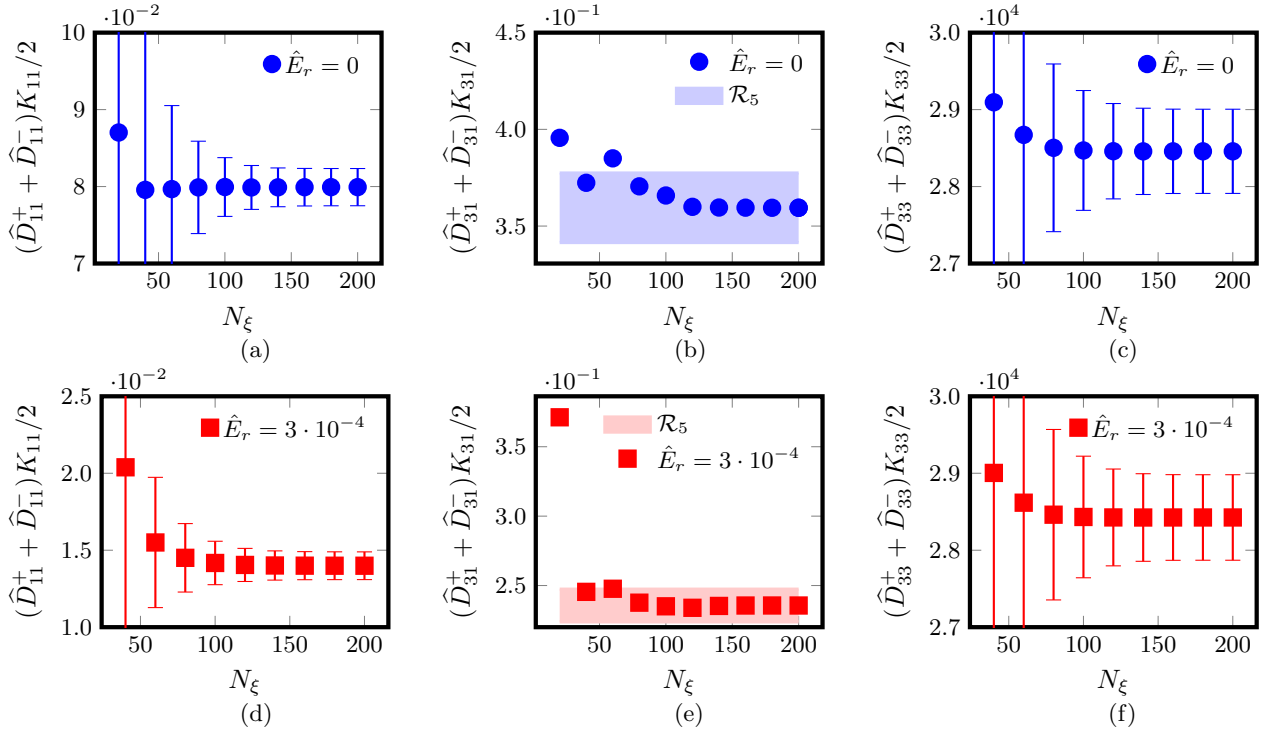


Figure D1: Convergence of monoenergetic coefficients calculated with DKES for W7X-EIM at the surface labelled by $\psi/\psi_{\text{lcf}} = 0.200$. \hat{E}_r in $\text{kV} \cdot \text{s}/\text{m}^2$.

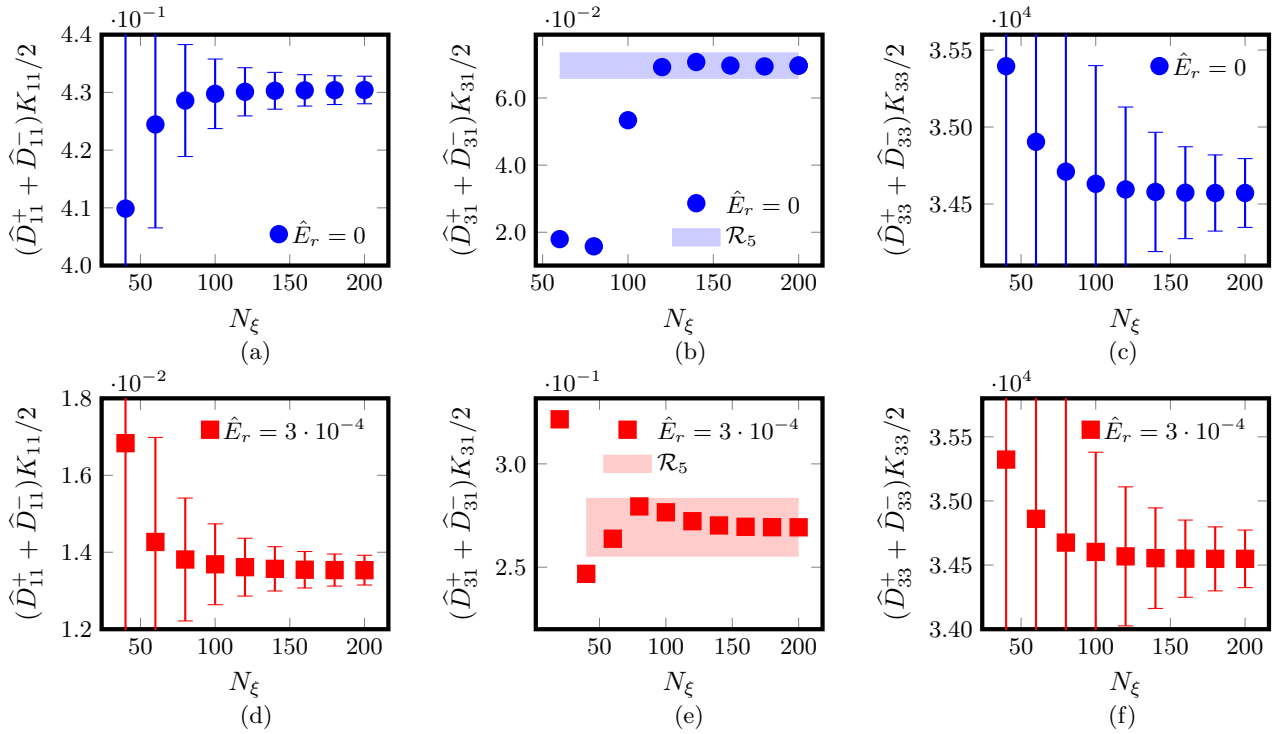


Figure D2: Convergence of monoenergetic coefficients calculated with DKES for W7X-KJM at the surface labelled by $\psi/\psi_{\text{lcf}} = 0.204$. \hat{E}_r in $\text{kV} \cdot \text{s}/\text{m}^2$.

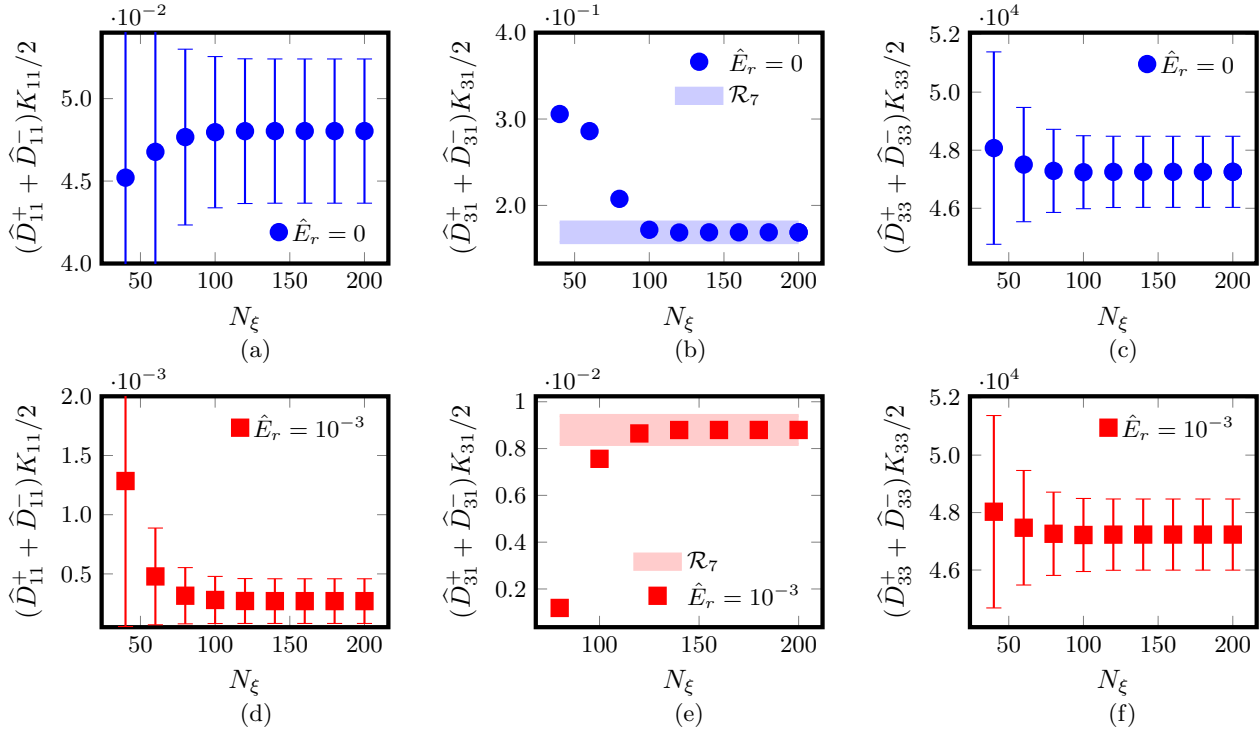


Figure D3: Convergence of monoenergetic coefficients calculated with DKES for CIEMAT-QI at the surface labelled by $\psi/\psi_{\text{lcs}} = 0.250$. \hat{E}_r in $\text{kV} \cdot \text{s/m}^2$.

Acknowledgements

References

- [1] J. R. Cary and S. G. Shasharina. Omnigenity and quasihelicity in helical plasma confinement systems. *Physics of Plasmas*, 4:3323–3333, 1997.
- [2] P. Helander and J. Nührenberg. Bootstrap current and neoclassical transport in quasi-isodynamic stellarators. *Plasma Physics and Controlled Fusion*, 51(5):055004, 2009.
- [3] P. Helander, J. Geiger, and H. Maaßberg. On the bootstrap current in stellarators and tokamaks. *Physics of Plasmas*, 18(9), 2011. 092505.
- [4] C. D. Beidler, H. M. Smith, A. Alonso, T. Andreeva, J. Baldzuhn, M. N. A. Beurskens, M. Borchardt, S. A. Bozhnikov, K. J. Brunner, H. Damm, M. Drevlak, O. P. Ford, G. Fuchert, J. Geiger, P. Helander, U. Hergenhan, M. Hirsch, U. Höfel, Ye. O. Kazakov, R. Kleiber, M. Krychowiak, S. Kwak, A. Langenberg, H. P. Laqua, U. Neuner, N. A. Pablant, E. Pasch, A. Pavone, T. S. Pedersen, K. Rahbarnia, J. Schilling, E. R. Scott, T. Stange, J. Svensson, H. Thomsen, Y. Turkin, F. Warmer, R. C. Wolf, D. Zhang, I. Abramovic, S. Äkäslompolo, J. Alcúsn, P. Aleynikov, K. Aleynikova, A. Ali, G. Anda, E. Ascasibar, J. P. Böhner, S. G. Baek, M. Balden, M. Banduch, T. Barbui, W. Behr, A. Benndorf, C. Biedermann, W. Biel, B. Blackwell, E. Blanco, M. Blatzheim, S. Ballinger, T. Bluhm, D. Böckenhoff, B. Böswhir, L.-G. Böttger, V. Borsuk, J. Boscary, H.-S. Bosch, R. Brakel, H. Brand, C. Brandt, T. Bräuer, H. Braune, S. Brezinsek, K.-J. Brunner, R. Burhenn, R. Bussiahn, B. Buttenschön, V. Bykov, J. Cai, I. Calvo, B. Cannas, A. Cappa, A. Carls, L. Carraro, B. Carvalho, F. Castejon, A. Charl,
- N. Chaudhary, D. Chauvin, F. Chernyshev, M. Cianciosa, R. Citarella, G. Claps, J. Coenen, M. Cole, M. J. Cole, F. Cordella, G. Cseh, A. Czarnecka, K. Czerski, M. Czerwinski, G. Czymek, A. da Molin, A. da Silva, A. de la Pena, S. Degenkolbe, C. P. Dhard, M. Dibon, A. Dinklage, T. Dittmar, P. Drewelow, P. Drews, F. Durodie, E. Edlund, F. Effenberg, G. Ehrke, S. Elgeti, M. Endler, D. Ennis, H. Esteban, T. Estrada, J. Fellingner, Y. Feng, E. Flom, H. Fernandes, W. H. Fietz, W. Figacz, J. Fontdecaba, T. Fornal, H. Frerichs, A. Freund, T. Funaba, A. Galkowski, G. Gantenbein, Y. Gao, J. García Regaña, D. Gates, B. Geiger, V. Giannela, A. Gogoleva, B. Goncalves, A. Gorlaev, D. Gradic, M. Grahl, J. Green, H. Greuner, A. Grosman, H. Grote, M. Gruca, O. Grulke, C. Guerard, P. Hacker, X. Han, J. H. Harris, D. Hartmann, D. Hathiramani, B. Hein, B. Heinemann, S. Henneberg, M. Henkel, J. Hernandez Sanchez, C. Hidalgo, K. P. Hollfeld, A. Hölting, D. Höschen, M. Houry, J. Howard, X. Huang, Z. Huang, M. Hubeny, M. Huber, H. Hunger, K. Ida, T. Ilkei, S. Illy, B. Israeli, S. Jablonski, M. Jakubowski, J. Jelonnek, H. Jenzsch, T. Jesche, M. Jia, P. Junghanns, J. Kacmarczyk, J.-P. Kallmeyer, U. Kamionka, H. Kasahara, W. Kasperek, N. Kenmochi, C. Killer, A. Kirschner, T. Klinger, J. Knauer, M. Knaup, A. Knieps, T. Kobarg, G. Kocsis, F. Köchl, Y. Kolesnichenko, A. Könies, R. König, P. Kornejew, J.-P. Koschinsky, F. Köster, M. Krämer, R. Krampitz, A. Krämer-Flecken, N. Krawczyk, T. Kremeyer, J. Krom, I. Ksiazek, M. Kubkowska, G. Kühner, T. Kurki-Suonio, P. A. Kurz, M. Landreman, P. Lang, R. Lang, S. Langish, H. Laqua, R. Laube, S. Lazerson, C. Lechte, M. Lennartz, W. Leonhardt, C. Li, Y. Li, Y. Liang, C. Linsmeier, S. Liu, J.-F. Lobsien, D. Loesser, J. Loizu Cissequella, J. Lore, A. Lorenz, M. Losert, A. Lücke, A. Lumsdaine, V. Lut-

- senko, H. Maaßberg, O. Marchuk, J. H. Matthew, S. Marsen, M. Marushchenko, S. Masuzaki, D. Maurer, M. Mayer, K. McCarthy, P. McNeely, A. Meier, D. Mellein, B. Mendelevitch, P. Mertens, D. Mikkelsen, A. Mishchenko, B. Missal, J. Mittelstaedt, T. Mizuuchi, A. Mollen, V. Moncada, T. Mönnich, T. Morisaki, D. Moseev, S. Murakami, G. Náfrádi, M. Nagel, D. Naujoks, H. Neilson, R. Neu, O. Neubauer, T. Ngo, D. Nicolai, S. K. Nielsen, H. Niemann, T. Nishizawa, R. Nocentini, C. Nührenberg, J. Nührenberg, S. Obermayer, G. Offermanns, K. Ogawa, J. Ölmanns, J. Ongena, J. W. Oosterbeek, G. Orozco, M. Otte, L. Pacios Rodriguez, N. Panadero, N. Panadero Alvarez, D. Papenfuß, S. Paqay, E. Pawelec, G. Pelka, V. Perseo, and the W7-X Team. Demonstration of reduced neoclassical energy transport in wendelstein 7-x. *Nature*, 596(7871):221–226, 2021.
- [5] A. Dinklage, C. D. Beidler, P. Helander, G. Fuchert, H. Maaßberg, K. Rahbarnia, T. Sunn Pedersen, Y. Turkin, R. C. Wolf, A. Alonso, T. Andreeva, B. Blackwell, S. Bozhnikov, B. Buttenschön, A. Czarnecka, F. Effenberg, Y. Feng, J. Geiger, M. Hirsch, U. Höfel, M. Jakubowski, T. Klinger, J. Knauer, G. Kocsis, A. Krämer-Flecken, M. Kubkowska, A. Langenberg, H. P. Laqua, N. Marushchenko, A. Mollén, U. Neuner, H. Niemann, E. Pasch, N. Pablant, L. Rudischhauser, H. M. Smith, O. Schmitz, T. Stange, T. Szepesi, G. Weir, T. Windisch, G. A. Wurden, D. Zhang, I. Abramovic, S. Äkäsłompolo, A. Ali, J. Alcúson Belloso, P. Aleynikov, K. Aleynikova, R. Alzbutas, G. Anda, E. Ascasibar, J. Assmann, S.-G. Baek, J. Baldzuhn, M. Banduch, T. Barbui, M. Barlak, K. Baumann, W. Behr, C. Beidler, A. Benndorf, O. Bertuch, M. Beurskens, C. Biedermann, W. Biel, D. Birus, E. Blanco, M. Blatzheim, T. Bluhm, D. Böckenhoff, P. Bolgert, M. Borchardt, V. Borsuk, J. Boscary, H.-S. Bosch, L.-G. Böttger, R. Brakel, H. Brand, Ch. Brandt, T. Bräuer, H. Braune, S. Brezinsek, K.-J. Brunner, B. Brünner, R. Burhenn, R. Bussiahn, V. Bykov, Y. Cai, I. Calvo, B. Cannas, A. Cappa, A. Card, A. Carls, L. Carraro, B. Carvalho, F. Castejon, A. Charl, F. Chernyshev, M. Cianciosa, R. Citarella, L. Ciupiński, G. Claps, M. J. Cole, F. Cordella, G. Cseh, A. Czermak, K. Czerski, M. Czerwinski, G. Czymek, A. da Molin, A. da Silva, G. Dammertz, A. de la Pena, S. Degenkolbe, P. Denner, T. Dittmar, C. P. Dhard, M. Dostal, M. Drevlak, P. Drewelow, Ph. Drews, A. Dudek, G. Dundulis, F. Durodie, P. van Eeten, G. Ehrke, M. Endler, D. Ennis, E. Erckmann, H. Esteban, T. Estrada, N. Fahrenkamp, J.-H. Feist, J. Fellingner, H. Fernandes, W. H. Fietz, W. Figacz, J. Fontdecaba, O. Ford, T. Fornal, H. Frerichs, A. Freund, M. Führer, T. Funaba, A. Galkowski, G. Ganzenbein, Y. Gao, J. García Regaña, M. Garcia-Munoz, D. Gates, G. Gawlik, B. Geiger, V. Giannella, N. Gierse, A. Gogoleva, B. Goncalves, A. Gorlaev, D. Gradic, M. Grahl, J. Green, A. Grosman, H. Grote, M. Gruca, O. Grulke, C. Guerard, P. Hacker, L. Haiduk, K. Hammond, X. Han, F. Harberts, J. H. Harris, H.-J. Hartfuß, D. Hartmann, D. Hathiramani, B. Hein, B. Heinemann, P. Heitzenroeder, S. Henneberg, C. Hennig, J. Hernandez Sanchez, C. Hidalgo, H. Hölbe, K. P. Hollfeld, A. Hölting, D. Höschen, M. Houry, J. Howard, X. Huang, M. Huber, V. Huber, H. Hunger, K. Ida, T. Ilkei, S. Illy, B. Israeli, A. Ivanov, S. Jablonski, J. Jagielski, J. Jelonek, H. Jenzsch, P. Junghans, J. Kacmarczyk, T. Kalitka, J.-P. Kallmeyer, U. Kamionka, R. Karalevicius, H. Kasahara, W. Kasparek, Y. Kazakov, N. Kenmochi, M. Keunecke, A. Khilchenko, C. Killer, D. Kinna, R. Kleiber, M. Knaup, A. Knieps, Th. Kobarg, F. Köchl, Y. Kolesnichenko, A. Könies, M. Köppen, J. Koshurin, R. Kosłowski, R. König, F. Köster, P. Kornejew, R. Koziol, M. Krämer, R. Krampitz, P. Kraszewski, N. Krawczyk, T. Kremeyer, Th. Krings, J. Krom, M. Krychowiak, G. Krzesinski, I. Ksiązek, G. Kühner, T. Kurki-Suonio, S. Kwak, M. Landreman, R. Lang, S. Langish, H. Laqua, H. P. Laqua, R. Laube, S. Lazerson, C. Lechte, M. Lennartz, W. Leonhardt, L. Lewerentz, Y. Liang, Ch. Linsmeier, S. Liu, J.-F. Lobsien, D. Loesser, J. Loizu Cisse, J. Lore, A. Lorenz, M. Losert, L. Lubyako, A. Lücke, A. Lumsdaine, V. Lutsenko, J. Maisano-Brown, O. Marchuk, M. Mardenfeld, P. Marek, S. Marsen, M. Marushchenko, S. Masuzaki, D. Maurer, K. McCarthy, P. McNeely, A. Meier, , and the W7-X Team. Magnetic configuration effects on the wendelstein 7-x stellarator. *Nature Physics*, 14(8):855–860, 2018.
- [6] C.D. Beidler, K. Allmaier, M.Yu. Isaev, S.V. Kasilov, W. Kernbichler, G.O. Leitold, H. Maaßberg, D.R. Mikkelsen, S. Murakami, M. Schmidt, D.A. Spong, V. Tribaldos, and A. Wakasa. Benchmarking of the mono-energetic transport coefficients—results from the international collaboration on neoclassical transport in stellarators (icnts). *Nuclear Fusion*, 51(7):076001, 2011.
- [7] E. Sánchez, J.L. Velasco, I. Calvo, and S. Mulas. A quasi-isodynamic configuration with good confinement of fast ions at low plasma beta. *Nuclear Fusion*, 63(6):066037, 2023.
- [8] J. L. Velasco, I. Calvo, E. Sánchez, and F. I. Parra. Robust stellarator optimization via flat mirror magnetic fields, 2023.
- [9] R. Jorge, G.G. Plunk, M. Drevlak, M. Landreman, J.-F. Lobsien, K. Camacho Mata, and P. Helander. A single-field-period quasi-isodynamic stellarator. *Journal of Plasma Physics*, 88(5):175880504, 2022.
- [10] K. Camacho Mata, G. G. Plunk, and R. Jorge. Direct construction of stellarator-symmetric quasi-isodynamic magnetic configurations. *Journal of Plasma Physics*, 88(5):905880503, 2022.
- [11] A. Goodman, K. Camacho Mata, S. A. Henneberg, R. Jorge, M. Landreman, G. Plunk, H. Smith, R. Mackenbach, and P. Helander. Constructing precisely quasi-isodynamic magnetic fields, 2022.
- [12] A. Pytte and A. H. Boozer. Neoclassical transport in helically symmetric plasmas. *The Physics of Fluids*, 24(1):88–92, 1981.
- [13] A. H. Boozer. Transport and isomorphic equilibria. *The Physics of Fluids*, 26(2):496–499, 1983.
- [14] M. Landreman and E. Paul. Magnetic fields with precise quasisymmetry for plasma confinement. *Phys. Rev. Lett.*, 128:035001, 2022.
- [15] P. Helander. Theory of plasma confinement in non-axisymmetric magnetic fields. *Reports on Progress in Physics*, 77(8):087001, 2014.
- [16] M. Landreman, S. Buller, and M. Drevlak. Optimization of quasi-symmetric stellarators with self-consistent bootstrap current and energetic particle confinement. *Physics of Plasmas*, 29(8), 2022. 082501.
- [17] F. Simon B. Anderson, Abdulgader F. Almagri, D. T. Anderson, Peter G. Matthews, Joseph N. Talmadge, and J. Leon Shohet. The helically symmetric experiment, (hsx) goals, design and status. *Fusion Technology*, 27(3T):273–277, 1995.
- [18] M. C. Zarnstorff, L. A. Berry, A. Brooks, E. Fredrickson, G.-Y. Fu, S. Hirshman, S. Hudson, L.-P. Ku, E. Lazarus, D. Mikkelsen, D. Monticello, G. H. Neilson, N. Pomphrey, A. Reiman, D. Spong, D. Strickler, A. Boozer, W. A. Cooper, R. Goldston, R. Hatcher, M. Isaev, C. Kessel, J. Lewandowski, J. F. Lyon, P. Merkel, H. Mynick, B. E. Nelson, C. Nührenberg, M. Redi, W. Reiersen, P. Rutherford, R. Sanchez, J. Schmidt, and R. B. White.

- Physics of the compact advanced stellarator ncxs. *Plasma Physics and Controlled Fusion*, 43(12A):A237, 2001.
- [19] V. V. Nemov, S. V. Kasilov, W. Kernbichler, and M. F. Heyn. Evaluation of $1/\nu$ neoclassical transport in stellarators. *Physics of Plasmas*, 6:4622–4632, 1999.
- [20] K. C. Shaing and J. D. Callen. Neoclassical flows and transport in nonaxisymmetric toroidal plasmas. *The Physics of Fluids*, 26(11):3315–3326, 1983.
- [21] N. Nakajima, M. Okamoto, J. Todoroki, Y. Nakamura, and M. Wakatani. Optimization of bootstrap current in a large helical system with $L = 2$, 1988.
- [22] P. Helander, F. I. Parra, and S. L. Newton. Stellarator bootstrap current and plasma flow velocity at low collisionality. *Journal of Plasma Physics*, 83(2):905830206, 2017.
- [23] I. Calvo, F. I. Parra, J. L. Velasco, and J. A. Alonso. The effect of tangential drifts on neoclassical transport in stellarators close to omnigenicity. *Plasma Physics and Controlled Fusion*, 59(5):055014, 2017.
- [24] V. d’Herbemont, F. I. Parra, I. Calvo, and J. L. Velasco. Finite orbit width effects in large aspect ratio stellarators. *Journal of Plasma Physics*, 88(5):905880507, 2022.
- [25] J.L. Velasco, I. Calvo, F.I. Parra, and J.M. García-Regaña. Knosos: A fast orbit-averaging neoclassical code for stellarator geometry. *Journal of Computational Physics*, 418:109512, 2020.
- [26] J.L. Velasco, I. Calvo, F.I. Parra, V. d’Herbemont, H.M. Smith, D. Carralero, T. Estrada, and the W7-X Team. Fast simulations for large aspect ratio stellarators with the neoclassical code knosos. *Nuclear Fusion*, 61(11):116013, 2021.
- [27] S. Lazerson, J. Schmitt, C. Zhu, J. Breslau, All STELLOPT Developers, and USDOE Office of Science. Stellopt, version 2.7.5, 2020.
- [28] A. Bañón Navarro, A. Di Siena, J.L. Velasco, F. Wilms, G. Merlo, T. Windisch, L.L. LoDestro, J.B. Parker, and F. Jenko. First-principles based plasma profile predictions for optimized stellarators. *Nuclear Fusion*, 63(5):054003, 2023.
- [29] M. Barnes, I. G. Abel, W. Dorland, T. Görler, G. W. Hammett, and F. Jenko. Direct multiscale coupling of a transport code to gyrokinetic turbulence codesa). *Physics of Plasmas*, 17(5):056109, 2010.
- [30] W. I. van Rij and S. P. Hirshman. Variational bounds for transport coefficients in three-dimensional toroidal plasmas. *Physics of Fluids B: Plasma Physics*, 1(3):563–569, 1989.
- [31] M. Landreman, H. M. Smith, A. Mollén, and P. Helander. Comparison of particle trajectories and collision operators for collisional transport in nonaxisymmetric plasmas. *Physics of Plasmas*, 21(4):042503, 2014.
- [32] P. Helander and D. J. Sigmar. *Collisional transport in magnetized plasmas*. Cambridge university press, 2005.
- [33] S. P. Hirshman, K. C. Shaing, W. I. van Rij, C. O. Beasley, and E. C. Crume. Plasma transport coefficients for nonsymmetric toroidal confinement systems. *The Physics of Fluids*, 29(9):2951–2959, 1986.
- [34] M. Landreman. The monoenergetic approximation in stellarator neoclassical calculations. *Plasma Physics and Controlled Fusion*, 53(8):082003, 2011.
- [35] M. Taguchi. A method for calculating neoclassical transport coefficients with momentum conserving collision operator. *Physics of Fluids B: Plasma Physics*, 4(11):3638–3643, 1992.
- [36] H. Maaßberg, C. D. Beidler, and Y. Turkin. Momentum correction techniques for neoclassical transport in stellarators. *Physics of Plasmas*, 16(7), 2009. 072504.
- [37] D. A. Spong. Generation and damping of neoclassical plasma flows in stellaratorsa). *Physics of Plasmas*, 12(5), 2005. 056114.
- [38] H. Sugama and S. Nishimura. How to calculate the neoclassical viscosity, diffusion, and current coefficients in general toroidal plasmas. *Physics of Plasmas*, 9(11):4637–4653, 2002.
- [39] L. N. Trefethen and J. A. C. Weideman. The exponentially convergent trapezoidal rule. *SIAM Review*, 56(3):385–458, 2014.
- [40] E. Anderson, Z. Bai, C. Bischof, S. Blackford, J. Demmel, J. Dongarra, J. Du Croz, A. Greenbaum, S. Hammarling, A. McKenney, and D. Sorensen. *LAPACK Users’ Guide*. Society for Industrial and Applied Mathematics, Philadelphia, PA, third edition, 1999.
- [41] J. L. Tennyson, J. R. Cary, and D. F. Escande. Change of the adiabatic invariant due to separatrix crossing. *Phys. Rev. Lett.*, 56:2117–2120, 1986.